16

Forest Biophysical and Biochemical Properties from Hyperspectral and LiDAR Remote Sensing

Gregory P. Asner
Carnegie Institution for Science

Susan L. Ustin
University of California, Davis

Philip A. Townsend
University of Wisconsin, Madison

Roberta E. Martin
Carnegie Institution for Science

K. Dana Chadwick
Carnegie Institution for Science

Acronyms and Definitions

ACD	Aboveground carbon density
AIS	Airborne imaging spectrometer
ALI	Advanced Land Imager
A_{max}	Maximum rate of photosynthesis
APAR	Absorbed photosynthetically active radiation
ATLAS	Advanced Topographic Laser Altimeter System
AVIRIS	Airborne visible/infrared imaging spectrometer
CAO	Carnegie Airborne Observatory
CASI	Compact Airborne Spectrographic Imager
CHRIS	Compact High-Resolution Imaging Spectrometer
DASF	Directional area scattering factor
EnMAP	Environmental Mapping and Analysis Program
EO-1	Earth Observing-1 (Hyperion)
ESA	European Space Agency
ETM+	Enhanced Thematic Mapper Plus
ETR	Electron transport rate
EWT	Equivalent water thickness
GLAS	Geoscience Laser Altimeter System
HSI	Hyperspectral imaging
HyspIRI	Hyperspectral and Infrared Imager
ICESat	Ice, Cloud, and land Elevation Satellite
J_{max}	Maximum electric transport rate
LAD	Leaf angle distribution
LAI	Leaf area index
LiDAR	Light detection and ranging
LMA	Leaf mass per area
LUE	Light use efficiency
LVIS	Land, Vegetation, and Ice Sensor
MCH	Mean canopy profile height
N	Nitrogen
NCALM	National Center for Airborne Laser Mapping
NDVI	Normalized difference vegetation index
NEON	National Ecological Observatory Network
NIR	Near infrared
NPP	Net primary productivity
NPQ	Nonphotochemical quenching
NPV	Nonphotosynthetic vegetation
NSF	National Science Foundation
PAR	Photosynthetically active radiation
PLSR	Partial least squares regression
PRI	Photochemical Reflectance Index
SIF	Solar-induced fluorescence
SLA	Specific leaf area
SNR	Signal-to-noise ratio

SWIR	Shortwave infrared
UAV	Unmanned aerial vehicle
V_{cmax}	Maximum rate of carboxylation
VNIR	Visible to near infrared
VSWIR	Visible to shortwave infrared

16.1 Introduction

Forests store about three-quarters of all carbon stocks in vegetation in the terrestrial biosphere and harbor an array of organisms that comprise most of this carbon (IPCC 2000). The distribution of carbon and biodiversity in forests is spatially and temporally heterogeneous. The complex, 3D arrangement of plant species and their tissues has always challenged field-based studies of forests. Remote sensing has long endeavored to address these challenges by mapping the cover, structure, composition, and functional attributes of forests, and new approaches are continually being developed to increase the breadth and accuracy of remote measurements.

Over the past few decades, two technologies—hyperspectral imaging (HSI) and light detection and ranging (LiDAR)—have rapidly advanced from use in testbed-type research to applications ranging from ecology to land management. HSI, also known as imaging spectroscopy, involves the measurement of reflected solar radiance in narrow, contiguous spectral bands that form a spectrum for each image pixel. LiDAR uses emitted laser pulses in a scanning pattern to determine the distance between objects such as canopy foliage and ground surfaces. Individually, HSI and LiDAR are advancing the study of forests at landscape to global scales, uncovering new spatial and temporal patterns of forest biophysical and biochemical properties, as well as physiological processes. When combined, HSI and LiDAR can provide ecological detail at spatial scales unachievable in the field. This chapter discusses HSI and LiDAR data sources, techniques, applications, and challenges in the context of forest ecological research.

16.2 HSI and LiDAR Data

16.2.1 HSI Data Sources

The availability of HSI for ecological applications is growing as the utility of these data has increasingly been recognized. HSI can be collected either with airborne sensors that have a limited spatial coverage but high-spatial resolution or with spaceborne sensors capable of capturing data globally, but generally with coarser spatial resolution. There are an expanding number of government, private, and commercial airborne HSI sensors. In addition, one spaceborne HSI sensor—Earth Observing-1 (EO-1) Hyperion—has been in operation as a technology demonstration since November 2000. Other orbital sensors are in the planning or development stages in hopes of further extending the spatial coverage of available imaging spectroscopy (Table 16.1).

Airborne HSI sensors have been operating since the 1980s. An early system was NASA's airborne imaging spectrometer (AIS), followed later by the airborne visible/infrared imaging spectrometer (AVIRIS), which is still in operation and provides data to NASA-supported investigators. Newer instruments including the Carnegie Airborne Observatory (CAO) visible-to-shortwave-infrared (VSWIR) imaging spectrometer provide increased spectral resolution and performance (e.g., signal-to-noise ratio [SNR]) over previous technology (Table 16.1). The U.S. National Science Foundation's (NSF) National Ecological Observatory Network (NEON) has created three copies of the CAO VSWIR, which will provide annual collection of HSI data for each of its core research sites across the United States.

Beyond government and privately funded instruments for research, a number of HSI sensors have been built for commercial applications. For example, the Compact Airborne Spectrographic Imager (CASI, CASI-2, CASI-1500) and HyMap provide high-performance visible-to-near-infrared (VNIR) (365–1052 nm) and VSWIR (440–2500 nm) measurements, respectively (Table 16.1).

TABLE 16.1 Examples of Current and Planned Airborne and Spaceborne HSI

Sensor	Spectral Range (nm)	Spectral Bands	Spectral Resolution (nm)	Spatial Resolution (m)	Reference
Airborne					
AVIRIS	400–2450	224	10	2.0+	Green et al. (1998)
AVIS-2	400–900	64	9	2.0+	Oppelt and Mauser (2007)
CAO VSWIR	380–2510	428	5	0.5+	Asner et al. (2012)
HYDICE	400–2500	206	8–15	1.0+	Basedow et al. (1995)
NEON VSWIR	380–2500	212	10	0.5+	www.neoninc.org
AISA	380–2500	275	3.5–12	1+	www.specim.fi
CASI	365–1052	288	2–10	0.25+	www.itres.com
HyMap	440–2500	100–200	10–20	2.0+	Cocks et al. (1998)
Spaceborne					
EO-1 Hyperion	400–2500	220	10	30	Folkman et al. (2001)
Proba-1 CHRIS	415–1050	18–62	1.3–12	18, 36	Barnsley et al. (2004)
EnMAP (*planned*)	420–2450	98–130	6.5–10	30	Stuffler et al. (2007)
HyspIRI (*planned*)	380–2500	210	10	60	hyspiri.jpl.nasa.gov

In comparison to airborne systems, there are fewer spaceborne sensors collecting hyperspectral data (Table 16.1). NASA's EO-1 Hyperion has far exceeded its intended 1-year life span, performing for over a decade (Riebeek 2010). Thenkabail et al. (2004) showed that Hyperion data, when compared to data from even the most advanced broadband sensors (Enhanced Thematic Mapper Plus [ETM+], IKONOS, and Advanced Land Imager [ALI]) in orbit at that time, yielded models that explained 36%–83% more of the variability in rainforest biomass and produced land use/land cover classifications with 45%–52% higher accuracies. The European Space Agency (ESA) also has a hyperspectral sensor (Compact High-Resolution Imaging Spectrometer [CHRIS]) on board the Proba-1 satellite, which observes in the visible and near-infrared (NIR) portion of the spectrum, though at higher spatial resolutions than Hyperion it is only able to record in 18 bands in this range (Barnsley et al. 2004). In addition, Germany is planning the launch of a hyperspectral sensor Environmental Mapping and Analysis Program (EnMAP) in 2017, and NASA is planning a mission called Hyperspectral and Infrared Imager (HyspIRI) for sometime near the year 2020. The addition of these spaceborne sensors will greatly contribute to the spatial and temporal coverage of hyperspectral data for forest research.

16.2.2 LiDAR Data Sources

LiDAR data sources are both numerous and variable, a reflection of the demand for airborne LiDAR in a wide variety of scientific and engineering applications. Recent and upcoming spaceborne LiDAR systems, described in this section, offer new data for forest monitoring. While the amount of LiDAR data being collected is increasing, there is a great deal of variability in the quality, type (discrete return vs. waveform), and spatial resolution of the resulting data.

LiDAR datasets for the United States are publicly available from a variety of sources. The National Center for Airborne Laser Mapping (NCALM; www.ncalm.cive.uh.edu) uses commercially sourced LiDAR sensors to collect high-resolution data (>2 laser spots m^{-2}) for NSF-funded projects or for other select projects. These data are currently made available to the public within 2 years of collection through the NSF-supported OpenTopography program (www.opentopography.org), which provides a platform to access these data, along with other LiDAR datasets contributed by researchers. NASA's Land, Vegetation, and Ice Sensor (LVIS), which has been operating in North America since the late 1990s, provides waveform data at coarser resolution of 10–25 m diameter laser spots in support of NASA studies (Blair et al. 1999). In addition, due to the increasing availability of commercial LiDAR acquisition services, many state and local governments have commissioned datasets. In the United States, the National Oceanic and Atmospheric Administration provides an inventory of these data (http://www.csc.noaa.gov/inventory/). There are no standard characteristics of these datasets, as they all vary with sensor parameters, elevation of data collection, and the density of returns collected. These heterogeneous data collection conditions hinder general assessments of the quality of these data.

In addition to airborne LiDAR data, NASA's Geoscience Laser Altimeter System (GLAS) Instrument, on board the Ice, Cloud, and land Elevation Satellite (ICESat), was the first spaceborne LiDAR instrument (Abshire et al. 2005). GLAS collected waveform data with 70 m spot diameter and 170 m spot intervals. The GLAS instrument was in operation from 2003 to 2009, and the data are publically available (icesat.gsfc.nasa.gov). The ICESat-2 is expected to launch in 2016, carrying the Advanced Topographic Laser Altimeter System (ATLAS).

16.2.3 Data Quality

The vast majority of HSI and LiDAR instruments have been deployed on aircraft, so the geographic coverage, ground sampling distance (spatial resolution and/or laser spot spacing), flying altitudes, and atmospheric conditions have varied enormously, making comparisons of instrument performances difficult to achieve. Nonetheless, comparative use of these instruments often reveals that sensor performance is paramount to achieving quality estimates of vegetation biophysical and biochemical properties.

Three sensor qualities have proven particularly important in the effort to achieve high-fidelity data output. These include detector uniformity, instrument stability, and SNR performance of the measurement (Green 1998). From the HSI perspective, each of these metrics of quality is important. Uniformity refers to the detailed way in which spectra are collected in the cross track and spectral directions on the instrument detector. Many HSI instruments fail to meet the often-cited 95%–98% absolute uniformity standard. One of the most insidious errors in uniformity occurs in the spectral direction. Most area-array HSI sensors fail to keep the spectral measurement aligned "down spectrum" from the VNIR (e.g., 400–1100 nm) and throughout the shortwave infrared (SWIR) (e.g., 1100–2500 nm), leading to a mismatch in different parts of the spectrum projected onto the Earth's surface. Another HSI performance issue is stability, which refers to the repeatability of the measurement across the imaging detector and/or over time. Much of the stability issue rests in the performance of the electronics and temperature stabilization subsystems. Finally, SNR is a quality that reports the strength and accuracy of the measurement signal relative to noise generated by the electronics and optics. SNR varies widely from instrument to instrument and also with environmental conditions such as temperature and humidity. Readers should be cautious when reviewing potential sources of HSI data, as providers may report SNR on either a bright target (e.g., white reference) or with enlarged camera apertures and/or inappropriately long integration times (equivalent to shutter speed). This will greatly inflate reported SNR values. For vegetation applications, SNR performances should be reported on dark targets in the 5%–8% reflectance range, typical for plants in the visible spectrum (350–700 nm), and with integration times that are appropriate for airborne or spaceborne ground speeds (usually 10 ms).

TABLE 16.2 Forest Biochemical and Physiological Properties Estimated from HSI, along with a Summary of Example Methods (Spectral Indices), Relevant Spectral Bands, Maturity, and References

Vegetation Property	Estimation Method(s)	Relevant Bands (nm)	Maturity Level	Example References
Foliar nitrogen	Normalized difference nitrogen index; band depth analysis; PLSR; RT model inversion	1510, 1680; 400–2500	✓✓	Kokaly (2001), Serrano et al. (2002), Smith et al. (2003), Asner and Vitousek (2005), and Dahlin et al. (2013)
LUE	PRI	531, 570	✓✓	Gamon et al. (1992, 1997), Gamon and Surfus (1999), Stylinksi et al. (2000), Guo and Trotter (2004), Hilker et al. (2008), Filella et al. (2009), Garbulsky et al. (2011), and Ripullone et al. (2011)
Foliar carotenoids	Various narrowband spectral indices	510, 550, 700; 445, 680, 800	✓✓	Gitelson et al. (2002) and Peñuelas et al. (1995)
Foliar anthocyanin	Various narrowband spectral indices	400–700	✓	Gamon and Surfus (1999), Gitelson et al. (2001, 2006), and Van den Berg and Perkins (2005)
APAR	Simple ratio, NDVI	400–700	✓✓✓	Jordan (1969) and Rouse et al. (1974)
LAI	Various narrowband spectral indices; RT model inversion	700–1300	✓✓✓	Rouse et al. (1974), Huete (1988), Gao et al. (1995), Rondeaux et al. (1996), Haboudane et al. (2002), Gitelson (2004), and Lim et al. (2004)
LMA	PLSR	400–2500	✓	Asner et al. (2011)
Foliar chlorophylls	Various narrowband spectral indices; RT model inversion	550, 670, 700; 800–1300; 690–725	✓✓✓	Kim (1994), Daughtry et al. (2000), Zarco-Tejada et al. (2001), Gitelson et al. (2006), and Zhang et al. (2008)
Foliar water	Various narrowband spectral indices	820, 1600; 860, 1240; 900, 970	✓✓	Hunt and Rock (1989), Peñuelas et al. (1997), and Dahlin et al. (2013)
Canopy water	EWT; RT model inversion	800–2500	✓✓✓	Hunt and Rock (1989), Gao and Goetz (1990), Gao (1996), Peñuelas et al. (1997), and Roberts et al. (2004)
Foliar lignin and cellulose	Cellulose absorption index; normalized difference lignin index	2015, 2106, 2195; 1680, 1754	✓✓	Daughtry (2001) and Serrano et al. (2002)
Foliar carbon	PLSR	1500–2500	✓	Dahlin et al. (2013)

Note: Maturity is a metric of relative accuracy as depicted in the literature, with one checkmark indicating low maturity and three checkmarks indicating high maturity. RT, radiative transfer; PLSR, partial least squares regression.

LiDAR measurements also have SNR, uniformity, and stability challenges. The shape, noisiness, and strength of the outbound laser pulses largely affect LiDAR SNR. Commercial LiDARs come in a wide range of SNR performance levels. For forest science, strong pulse strength (e.g., high-wattage laser diodes) is necessary to overcome absorption by the vegetation canopy. In addition, uniformity tends to be overlooked by scientists prior to data source selection; it is highly advisable to select LiDAR instruments that deliver a uniform scan pattern across the swath of the data set. Without strict control over this factor, the user will end up with high data density in the middle of the scan and low-data density at the edges of the scan. Finally, stability is a key issue with LiDAR instrumentation. Many commercial LiDARs exhibit instability as they change temperature, pressure, and humidity, resulting in variability in the quality of the laser data throughout the course of a mapping flight or research campaign.

16.3 HSI Remote Sensing of Forests

Forests, as fundamental components of the Earth's biosphere, have been a major focus of study from the beginning of HSI data collection. HSI provides a quantitative measure of the sunlight reflected from the forest canopy and the properties therein. The extended range and high-fidelity narrowband resolution of HSI offers enhanced capability for mapping forest biochemical and biophysical constituents along with physiological processes that contribute to the shape of the reflectance spectrum (Table 16.2). HSI data are used in a number of ways to assess leaf and canopy properties, namely, semiempirical methods utilizing narrowband spectral indices, regression modeling, and radiative transfer model inversion. As the HSI data quality improves, so do the results derived from these methods. Most recently, HSI combined with improved analytical methods has dramatically advanced species mapping and land cover classification.

16.3.1 Biophysical Properties

HSI data can uncover biophysical properties of ecological significance at both the leaf and canopy scales. Properties related to forest composition and leaf area index (LAI) are perhaps best retrieved from HSI data, whereas some properties like canopy-gap distribution and leaf angle distribution (LAD) are more readily determined from LiDAR. LAI (leaf area per unit ground area, $m^2\ m^{-2}$) is one of the most important canopy properties because it is directly related to productivity and water use, but variation in LAI can also indicate stress resistance and competition for light (see Waring 1983; Asner et al. 2004a). Field data and models show that LAI and LAD are primary controls on canopy reflectance in dense vegetation (Gong et al. 1992; Asner 1998).

While LAI is detectable from broadband sensors, studies show that HSI data and analysis methods optimized for HSI are more accurate (e.g., Spanner et al. 1994; Gong et al. 1995). Lee et al. (2004) examined four structurally different land cover types and showed that HSI red-edge and SWIR bands produced the best estimates of LAI. Equivalent water thickness (EWT, mm) produces better estimates of LAI than do pigment-based indices such as the normalized difference vegetation index (NDVI) (Roberts et al. 1998), with LAI values (up to nine) that far exceed the sensitivity range of NDVI and other indices (Roberts et al. 2004). Water indices derived from HSI have also been used to quantify loss of LAI from pest-related defoliation and other factors (e.g., White et al. 2007).

At the leaf level, leaf mass per area (LMA, g m^{-2} and its reciprocal; specific leaf area [SLA], m^2 g^{-1}) is a key foliar property that is highly correlated with light harvesting and potential plant productivity (Niinemets 1999; Westoby et al. 2002). LMA can be defined for foliage throughout the canopy or in any given canopy layer, depending upon the ecological question. While there is enormous range in LMA within a given plant functional type and among coexisting species, LMA is broadly correlated with temperature and precipitation at the global level (Wright et al. 2004). Higher temperatures, drier conditions, and higher irradiance are associated with higher values of LMA. Leaves with higher LMA are built for defense and longer life spans, creating higher resource use efficiency per nutrient acquired (Poorter et al. 2009). Conversely, lower LMA values are found in fast-growing species, often with higher nutrient concentrations and photosynthetic rates (Wright et al. 2004). In addition, there is a strong degree of taxonomic organization to LMA within forest communities (Asner et al. 2014). Because LMA is a function of leaf thickness and is correlated with total carbon and nitrogen, it is uniquely detectable in HSI data and has been estimated from inversion of radiative transfer models such as the PROSPECT model (Jacquemoud et al. 2009), chemometric analytical methods (Asner et al. 2011), and HSI-optimized SWIR indices (le Maire et al. 2008). The results from these studies conform to field measurements.

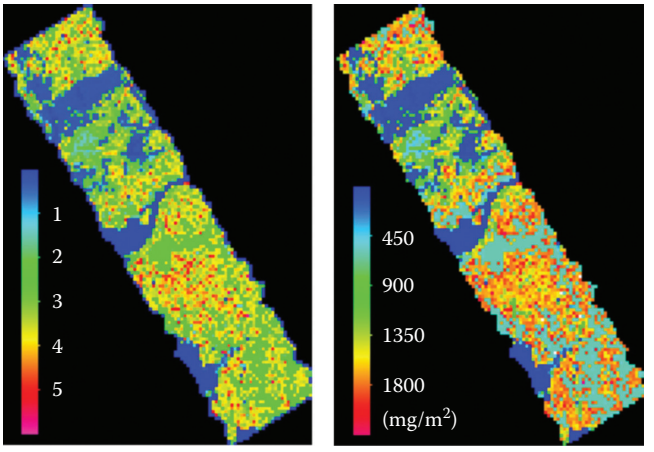

FIGURE 16.1 (a) LAI image of a black spruce forest (53.2% conifer, 16.1% deciduous species, and 21.1% grass) near Sudbury, Ontario, Canada. The image is derived based on a relationship between the simple ratio (near infrared/R) and LAI ($r^2 = 0.88$). (b). Chlorophyll a + b content distribution per unit ground area. The image combines the retrieved leaf chlorophyll a + b content for the three cover types ($r^2 = 0.47$) times the LAI. The chlorophyll data were analyzed using the 4-Scale geometrical–optical model to characterize the effect of structure on above canopy reflectance and inversion of the PROSPECT leaf model to estimate pigment concentration. Data from 72-band Compact Airborne Spectrographic Imager (HSI) averaged from 2 m pixel resolution to 20 m. (Reprinted from Zhang, Y. et al., *Remote Sens. Environ.*, 112, 3234, 2008.)

16.3.2 Biochemical Properties

The foremost motivation for biochemical detection is to better assess the spatiotemporal status and trends of forest canopy functioning, especially those related to fluxes of water, carbon, and nutrients. The list of plant biochemicals that have been identified and quantified using HSI data is extensive (Table 16.2) and has received several detailed reviews (Blackburn 2007; Kokaly et al. 2009; Ustin et al. 2009; Homolová et al. 2013). Many studies have found strong correlations between remotely sensed foliar nitrogen content and photosynthetic capacity or net primary production (Kokaly et al. 2009; Townsend et al. 2013), despite the small fraction of biomass comprised nitrogen. Most of these studies have been based on partial least squares regression (PLSR) analysis (Ollinger et al. 2002; Smith et al. 2002; Martin et al. 2008) of the full spectrum or spectral matching and continuum removal techniques (Kokaly 2001). Feilhauer et al. (2011) and Homolová et al. (2013) show that multiple wavelengths throughout the 400–2500 nm range have enabled nitrogen detection, indicating that nitrogen-related spectral features may vary by site, species, or phenological state.

Vegetation indices (Zarco-Tejada et al. 1999, 2001), semiempirical indices (e.g., Gitelson et al. 2003, 2006), and radiative transfer models (Zarco-Tejada et al. 2001, 2004; Féret et al. 2008, 2011) have been used to characterize growth-related foliar chemicals (e.g., nitrogen and chlorophyll pigments), yet other studies demonstrate that remote sensing of canopy structure also aids quantitative retrieval of biochemical properties (e.g., Zhang et al. 2008; Hernández-Clemente et al. 2012; Knyazikhin et al. 2013a,b,c; Ollinger et al. 2013; Townsend et al. 2013) (Figure 16.1). Asner and Warner (2003) conclude that quantitative information on gap fraction and tree structure is needed to validate or constrain remote sensing models to accurately estimate chemistry and energy exchange. Possible ways to account for structure in the retrieval of foliar chemistry include canopy radiative transfer models, LiDAR, and other methods that account for intra- and intercanopy gaps, self-shading, and stand structure (see Section 16.5.1). Many proposed methods remain untested, including the directional area scattering factor (DASF), which is a function based on three wavelength invariant parameters: canopy interceptance, probability of recollision, and directional gap density (Lewis and Disney 2007; Schull et al. 2007, 2011; Knyazikhin et al. 2013a). Still other researchers have argued that

the canopy architecture of a species is an integrated component of its strategy for resource capture and therefore should covary with chemistry (Ollinger et al. 2013; Townsend et al. 2013).

Foliar and canopy water content has also received a significant amount of attention due to its relationship with transpiration and plant water stress (Ustin et al. 2012; Hunt et al. 2013). The water absorption signal has a large effect on plant spectra, from small absorptions in the NIR at 970 and 1240 nm, accessible through HSI data, to a large broad absorption across the entire SWIR (1300–2500 nm). Gao and Goetz (1995) developed one of the first narrowband indices for the quantification of EWT of vegetation. The values derived for EWT from AVIRIS data were tested against field data from the Harvard Forest, Massachusetts. HSI also offers the unique ability to differentiate between different phases of water (atmospheric water vapor and the moisture content of vegetation), for which the absorption maxima are offset by about 40–50 nm (Gao and Geotz 1990). This ability to quantify atmospheric water aids in the statistical modeling of the atmosphere such that water vapor signals can be removed, permitting proper estimation of the underlying liquid water stored in vegetation (Green et al. 1989). Recently, Cheng et al. (2013b) showed that it is possible to monitor small diurnal changes in water content from optimized indices and wavelet analysis that provide information on plant water status and whether root uptake can support full transpiration demand.

Nonpigment materials in the forest canopy range from foliar carbon constituents, such as lignin and cellulose, to dead leaves, stems, or remaining reproductive structures of flowers and fruits. The detection and quantification of these materials, sometimes referred to as dry matter or nonphotosynthetic vegetation (NPV), is often used as an indicator of canopy stress and may be important for quantifying the contribution of plant litter to forest carbon pools. Particularly after foliage has lost pigments and water, the cellulose–lignin absorptions become easily detectable with HSI data through narrowband methods such as the cellulose absorption index (Daughtry 2001; Daughtry et al. 2005), spectral mixture analysis (Asner and Lobell 2000; Roberts et al. 2003a), chemometric approaches like PLSR (Asner et al. 2011), or radiative transfer models (Riaño et al. 2004; Jacquemoud et al. 2009). Kokaly et al. (2007, 2009) used continuum removal combined with a spectral library to reveal a 2–3 nm shift in the cellulose–lignin absorption feature when the concentration of lignin increases, demonstrating the utility of HSI in quantifying subtle variations in canopy carbon. Numerous examples of forest NPV quantification also exist in the HSI literature (e.g., Ustin and Trabucco 2000; Roberts et al. 2004; Guerschman et al. 2009). Dry matter signatures in the HSI spectrum have been used to assess whether canopies were subjected to insect defoliation, drought stress (White et al. 2007; Fassnacht et al. 2014), or root pathogen damage (Santos et al. 2010).

HSI data have significant potential for mapping forest composition at species and community levels, based largely on their biochemical attributes (Figure 16.2). Many examples have been published using various analytical approaches with airborne HSI images (e.g., Martin et al. 1998; Clark et al. 2005; Bunting and Lucas 2006; Bunting et al. 2010), EO-1 Hyperion satellite data (Townsend and Foster 2002), time series of Hyperion data (Kalacska et al. 2007; Somers and Asner 2013), and combinations of airborne HSI imagers and LiDAR (Dalponte et al. 2007; Jones et al. 2010; Colgan et al. 2012a; Naidoo et al. 2012; Baldeck et al. 2014). In recent years, the ability to map species and detailed land cover has significantly

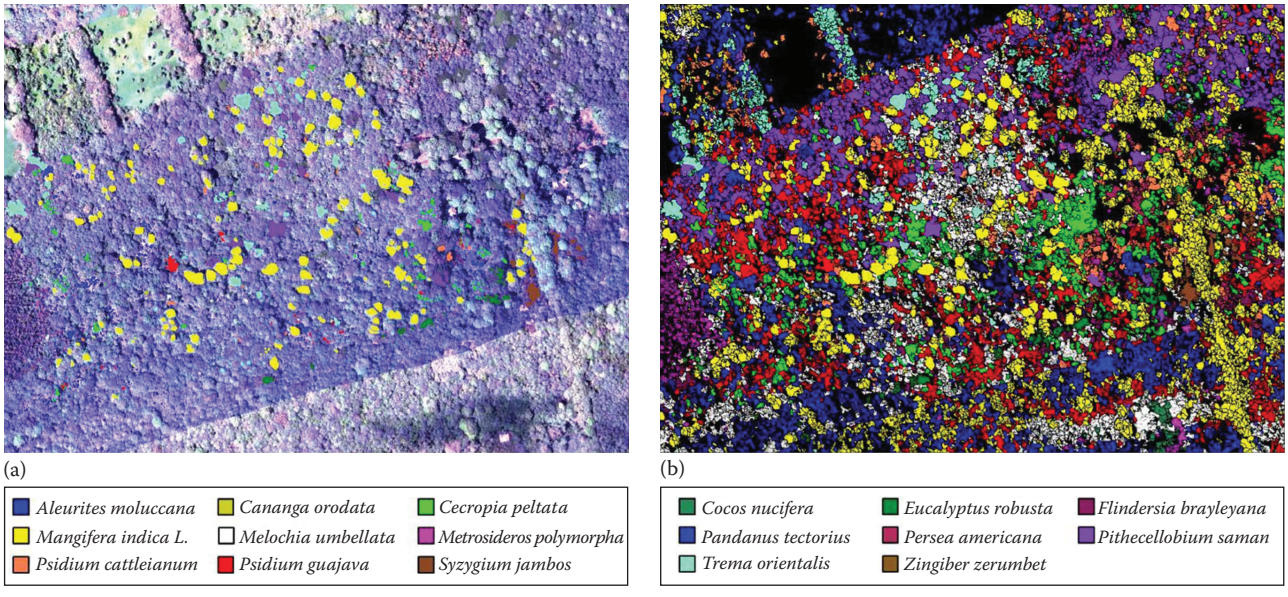

FIGURE 16.2 (a) A false color composite image of Nanawale Forest Reserve, Hawaii Island (R = 646 nm; G = 560.7 nm; B = 447 nm), with colored polygons showing locations of species data from a field survey. (b) Classification of 17 canopy species based on regularized discriminant analysis (n = 50 samples/species) using CAO VNIR imaging spectrometer data. (Reprinted from Féret, J.-B. and Asner, G.P., *Remote Sens. Environ.*, 115, 2415, 2013).

improved (Asner 2013). It is likely that this is a consequence of improved instrument performance, especially for high-fidelity HSI data and for the adoption of a wide variety of new analytical methods including radiative transfer models, segmentation and object delineation, and numerous statistical methods such as ensemble classifiers, discriminate analysis, support vector machines, and combined approaches. No one method has yet been shown to work universally across global land cover types with complex environment and terrain interactions. However, several general conclusions can be inferred from these and other studies: (1) the addition of SWIR bands along with VNIR bands often significantly increases the accuracy of mapping forest species; (2) species mapping is further enhanced if HSI data encompass multidate periods that capture phenological patterns, as is consistent with improvements reported for multidate multispectral data (e.g., Wolter et al. 2008); and (3) combining information on tree structure from LiDAR, such as canopy height, diameter, and volume, with HSI data improves results (Féret and Asner 2013).

16.3.3 Canopy Physiology

Imaging spectroscopy can be used to characterize three key physiological processes responsible for carbon uptake in forests: photochemistry, nonphotochemical quenching (NPQ), and fluorescence. Solar radiation, and photosynthetically active radiation (PAR; 400–700 nm) in particular, supplies the energy that drives carbon uptake in forests. The first process, photochemistry, refers directly to the process by which the enzyme ribulose-1,5 bisphosphate carboxylase–oxygenase (RuBisCO) catalyzes RuBP to fix carbon from carbon dioxide. Within the Calvin cycle of C_3 plants (which includes trees), photochemistry is driven by the energy supplied from light harvesting by pigment complexes. The second process, NPQ, relates directly to plant interactions with light. Plants downregulate photosynthesis through a range of processes related to pigment concentrations to either make use of light energy or dissipate it (Demmig-Adams and Adams 2006). Photochemistry and NPQ processes can be characterized through estimation of pigment concentrations or through inference based on changes in leaf pigment pools associated with plant responses to excess light or stresses that prevent them from fully utilizing ambient light energy (Demmig-Adams and Adams 1996). Finally, all plants dissipate light energy through solar-induced fluorescence (SIF), which only occurs as a consequence of photosynthesis and has been found to scale directly to rates of photosynthetic activity (Baker 2008).

Quantifying foliar nitrogen, the key element in RuBisCO and a trait whose concentration within proteins in foliage scales directly with photosynthetic capacity (Field and Mooney 1986; Evans 1989; Reich et al. 1997), provides a measure of the functioning of forest canopies (as described earlier). This functioning includes the capacity for carbon uptake, but photosynthetic downregulation limits carbon uptake under adverse environmental conditions. The most widely used models of photosynthesis employ the Farquhar model (Farquhar et al. 1980; Farquhar and von Caemmerer 1982), in which the potential photosynthetic performance of a leaf is characterized using two parameters: the maximum rate of carboxylation (V_{cmax}) governed by RuBisCO activity and the maximum electron transport rate (ETR) (J_{max} is the maximum rate of ETR; Farquar and von Caemmerer 1982). Together, these limit the maximum rate of photosynthesis (A_{max}). V_{cmax} is strongly related to N concentration and LMA, that is, the investment by a plant in light harvesting relative to construction and maintenance (Poorter et al. 2009). ETR and J_{max} are more closely related to the processes set in motion by light harvesting in PSI and PSII (PS = photosystem), necessary for the synthesis of adenosine triphosphate (ATP) to drive cellular reactions. Because the Calvin cycle depends on ATP availability to sustain the regeneration of RuBP (which in turn permits carboxylation), photosynthetic capacity is limited by J_{max}. Therefore, the optical properties of foliage related to light harvesting may also facilitate mapping J_{max} from HSI. It should be noted that all photosynthetic parameters of vegetation are sensitive to temperature and moisture, so any remotely sensed estimate of such parameters will be specific to the ambient conditions at the time of measurement (Serbin et al. 2012). HSI has also been used as part of multisensor approaches to characterize net ecosystem photosynthesis (e.g., Rahman et al. 2001; Asner et al. 2004a; Thomas et al. 2006, 2009).

Doughty et al. (2011) successfully related leaf-level spectroscopic measurements to A_{max} but had less success with the other parameters. Variations in V_{cmax} and J_{max} related to temperature were measured in cultivated aspen and cottonwood leaves and accurately predicted similar relationships in plantation trees (Serbin et al. 2012). The ability to map V_{cmax} and J_{max} from imaging spectroscopy is most likely a consequence of the ability to infer these properties from traits that are directly detectable based on known or hypothesized absorption features (e.g., N, LMA, and water; see Kattge et al. 2009 and Cho et al. 2010) and the coordination of these traits with canopy structure (Ollinger et al. 2013). These studies show promise for developing remote sensing methods to map the properties used by modelers to characterize forest physiological function.

Efforts to map parameters directly associated with photochemistry are an area of continuing development in imaging spectroscopy. The discipline of physiological remote sensing using HSI has its roots in efforts to characterize NPQ and how NPQ relates to photosynthetic rates and capacity. This work stems from the development of the Photochemical Reflectance Index (PRI) (Gamon et al. 1992; Peñuelas et al. 1995). While typically associated with the de-epoxidation of xanthophylls for photosynthetic downregulation during NPQ (Bilger and Björkman 1990; Demmig-Adams and Adams 1996), the PRI more generally correlates with total pigment pools and their variation with environmental context (Gamon and Bond 2013). As such, the PRI has been shown to be an indicator of photosynthetic rates and light use efficiency (LUE) (Gamon and Surfus 1999).

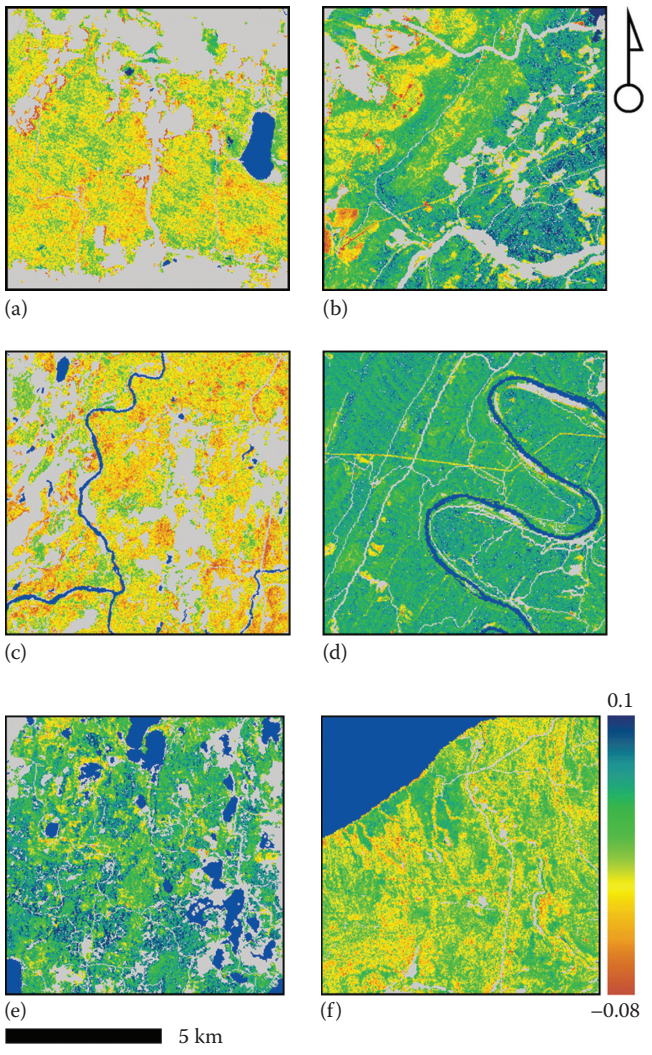

FIGURE 16.3 Midsummer PRI images derived from 2009 AVIRIS of (a) oak/pine forests in Baraboo/Devil's Lake, Wisconsin; (b) oak and tulip poplar forests in Fernow Experimental Forest, West Virginia; (c) northern hardwood and conifer forests in Flambeau River State Forest, Wisconsin; (d) xeric oak forests in Green Ridge State Forest, Maryland; (e) northern hardwood and subboreal conifers in Ottawa National Forest, Michigan; and (f) hemlock, white pine, and deciduous hardwoods in the Porcupine Mountains, Michigan. Lower values indicate areas of greater vegetation stress. These images illustrate significant variability in forest physiological status across landscapes.

Accounting for species composition, environmental variability, and seasonal responses, the PRI is often correlated with the carotenoid to chlorophyll ratio ($r^2 = 0.50–0.80$), a property linked to photosynthesis and light harvesting (Garbulsky et al. 2011) (Figure 16.3). In addition, Stylinksi et al. (2000) also showed close relationships between the PRI and xanthophyll cycle pigments and modeled electron transport capacity (J_{max}) in leaves of pubescent oak (*Quercus pubescens*). Kefauver et al. (2013) showed strong relationships between PRI and physiological damage to forests by ozone. A limitation of the PRI has been its species-level sensitivity, that is, relationships between the PRI and photosynthesis are species dependent (Guo and Trotter 2004; Filella et al. 2009; Ripullone et al. 2011). However, Hilker et al. (2008) have shown that PRI data may facilitate retrieval of plant photosynthetic efficiency independent of species composition.

The key physiological processes responsible for productivity of forests can also be addressed by remote sensing through the estimation of light absorption by canopies and its presumed linkage to light harvesting and use in photosynthesis. Under nonstressed conditions, net primary production is linearly related to the absorbed photosynthetically active radiation (APAR; Montieth 1977). This relationship is modulated by LUE. Traditionally, APAR has been successfully calculated from vegetation indices derived from spectral sensors of many varieties (e.g., Field et al. 1995; Sellers et al. 1996). The detection of forest LUE using PRI, and thus potential carbon uptake, has been demonstrated in numerous systems including boreal (Nichol et al. 2000) and conifer forests (Middleton et al. 2009; Atherton et al. 2013), but the utilization of remotely estimated APAR by the canopy for photosynthesis remains a more difficult task. The most common approach to assessing LUE using HSI has been through narrowband indices such as the PRI, which uses the reflectance at 570 and 531 nm (i.e., Gamon et al. 1997), but future developments in retrieving the Farquhar parameters (V_{cmax}, J_{max}) and SIF are likely to provide more robust estimates of key drivers of physiological processes. Ultimately, linkages across methods, for example, estimating LUE using derivations biochemistry (%N) and LAI, may provide a hybrid approach to best map factors important to net primary productivity (NPP) (Green et al. 2003).

Chlorophyll fluorescence provides another means of estimating photosynthetic performance and LUE from HSI data (Meroni et al. 2009). Numerous studies since the early 2000s have demonstrated the capacity of measurements of SIF to accurately characterize seasonal patterns of carbon uptake (Guanter et al. 2007; Frankenburg et al. 2011; Joiner et al. 2011). Under natural conditions, fluorescence and photosynthesis are positively correlated. Energy absorbed in the photosystems is reradiated at longer wavelengths than those absorbed, adding a subtle signal to reflected solar radiation, most notably with peaks around 685 and 740 nm. Measurements of SIF require narrowband data at specific wavelengths in the NIR in which the vegetation fluorescence signal in retrieved reflectance (about 2%) can be distinguished from NIR albedo (>40%) (Berry et al. 2013). Most efforts to date have focused on retrievals of SIF in narrow wavebands (preferably <0.3 nm) ± 20 nm around the solar Fraunhofer lines (wavelengths where there is no incoming solar energy, ~739 nm) or O_2-A band at 760 nm. Generally correlated with the PRI (Zarco-Tejada et al. 2009; Cheng et al. 2013a), fluorescence has also been measured at field sites differing in soil salinity and estimated

spatially from airborne HSI data using the PRI index (531 and 570 nm) (Naumann et al. 2008). Zarco-Tejada et al. (2009) estimated fluorescence from infilling of the O_2-A bands at 757.5 and 760.5 nm measured in 1 nm wavelength bands, which minimized confounding effects from variance in chlorophyll and LAI. More recently, Zarco-Tejada et al. (2013) used narrowband spectral indices and fluorescence infilling at 750, 762, and 780 nm, revealing that seasonal spectroscopic trends tracked changes in carbon fluxes. HSI observations continue to pave additional avenues to insight on plant physiological processes.

16.4 LiDAR Remote Sensing of Forests

Whereas HSI provides estimates of the chemical, physiological, and plant compositional properties of forests, LiDAR probes the structural and architectural traits of vegetation as well as the terrain below the canopy (Table 16.3). A large number of synthesis papers have been written on the use of LiDAR for studies of ecosystem structure (e.g., Dubayah and Drake 2000; Lefsky et al. 2002; Lim et al. 2003; Vierling et al. 2008; Wulder et al. 2012), including in other chapters of this book (e.g., Chapter 17). Here, we only briefly highlight the various uses of LiDAR in the context of forest structure, architecture, and biomass; the reader should also read Chapter 17 for further details.

16.4.1 Canopy Structure and Biomass

The height of a forest canopy is a fundamental characteristic that both discrete and waveform LiDAR sensors are capable of describing (Figure 16.4). Even discrete-return datasets that contain only the first and last return from the laser pulse will allow for the calculation of this parameter, after a ground elevation model has been generated from LiDAR data (Lim et al. 2003). While canopy height alone does not provide extensive information on forest structure, it is a parameter related to tree diameters (Feldpausch et al. 2012), and thus to aboveground biomass.

LiDAR can also be used to determine the vertical profile of canopy tissues including foliar and some woody structures (Figure 16.5). Waveform LiDAR instruments collect the full shape of the returning laser pulse, allowing for detailed information on the structure of the canopy (Blair and Hofton 1999; Dubayah and Drake 2000; Ni-Meister et al. 2001). If detailed canopy structure is of interest, but only discrete-return LiDAR data are available, it is possible to use these data to generate a pseudowaveform. This method aggregates discrete returns into bins over spatial extents that incorporate multiple laser spots in order to gain an aggregated understanding of the vertical vegetation profile in the absence of waveform data for each laser pulse (Muss et al. 2011). Vertical profiles are indicative of canopy density, vertical distribution, and the presence of undergrowth, all of which can provide information on the 3D structure and habitat of forests (Parker 1995; Lefsky et al. 1999; Clark and Clark 2000; Weishampel et al. 2000; Drake et al. 2002; Asner et al. 2008; Vierling et al. 2008).

One of the most widespread uses for LiDAR-derived canopy information is in the estimation of aboveground biomass, also known as aboveground carbon density (ACD). Such approaches have been applied in numerous studies of conifer, broadleaf temperate, and tropical forest ecosystems (Nelson 1988; Lefsky et al. 1999, 2002, 2005; Popescu et al. 2003; Næsset and Gobakken 2008; van Aardt et al. 2008; Asner et al. 2012c; Wulder et al. 2012). The mean canopy profile height (MCH) has been used as the canopy structural metric, which relates the LiDAR vertical structure data to ACD (Lefsky et al. 2002; Asner et al. 2009). However, recent studies have indicated that variations in sensor characteristics and settings can cause significant differences in the MCH metric between data acquisitions (Næsset 2009), strongly indicating that top-of-canopy height is a more reliable method for estimating ACD of tropical forests (Asner and Mascaro 2014). The use of LiDAR data to produce estimates of ACD that closely match plot-level estimates allows for the mapping and monitoring of aboveground carbon stocks at landscape scales and, with the further development of spaceborne LiDAR, potentially regional/biome scales.

TABLE 16.3 Forest Structural Properties Estimated from LiDAR, along with an Estimate of Scientific Maturity and Example References

Vegetation Property	Maturity Level	Example References
Total canopy height	✓✓✓	Dubayah and Drake (2000), Ni-Meister et al. (2001), Drake et al. (2002), and Lim et al. (2003)
Mean canopy profile height	✓✓✓	Lefsky et al. (1999, 2002, 2005)
Aboveground biomass	✓✓	Nelson (1988), Lefsky et al. (1999, 2002, 2005), Popescu et al. (2003), Næsset and Gobakken (2008), van Aardt et al. (2008), Asner et al. (2012c), and Wulder et al. (2012)
Leaf area density	✓	Sun and Ranson (2000), Lovell et al. (2003), Riaño et al. (2004), Morsdorf et al. (2006), Richardson et al. (2009), Soldberg et al. (2009), and Vaughn et al. (2013)
Understory presence	✓✓	Zimble et al. (2003) and Asner et al. (2008)

Note: Maturity is a metric of relative accuracy as depicted in the literature, with one checkmark indicating low maturity and three checkmarks indicating high maturity.

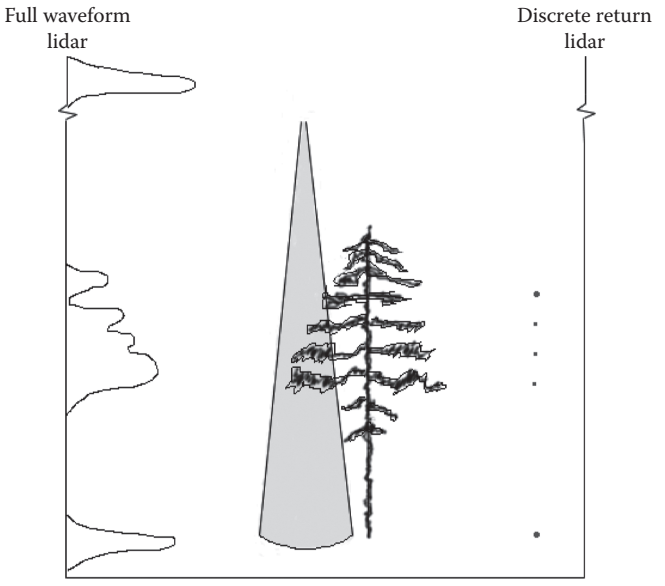

FIGURE 16.4 Illustration of waveform and discrete-return measurements of a tree. While both provide information on the vertical structure of canopies, discrete-return sampling records the returning laser pulse at specified peaks (e.g., first and last pulse) of the return wave, whereas waveform sampling collects the full shape of the returning pulse. (Reprinted from Lim, K. et al., *Prog. Phys. Geogr.*, 27, 88, 2003).

16.4.2 Light Penetration

Canopy gaps, or openings in forest canopies, influence population dynamics of forest trees by affecting forest structure, regeneration dynamics, and species composition (Brokaw 1985; Denslow 1987). Canopy gaps occur at scales ranging from single branches to multiple treefalls and result from disturbances caused by natural tree life cycles (Asner 2013), human processes such as logging (e.g., Nepstad et al. 1999; Asner et al. 2004b; Curran et al. 2004), and environmental factors such large-scale blowdowns (Chambers et al. 2013). Recently, airborne LiDAR data from a number of tropical forests have enabled the measurement of millions of canopy gaps over large spatial scales, both as single measurements and with repeat collections, improving the understanding of static and dynamics gaps, respectively (e.g., Magnussen et al. 2002; Kellner et al. 2009; Udayalakshmi et al. 2011; Armston et al. 2013).

Static canopy-gap size-frequency distributions (known as λ) are strikingly similar across a wide range of tropical forest types on differing geologic substrates and within differing disturbance regimes. This collective evidence suggests consistent turnover rates and similar mechanisms of gap formation across tropical forests (Kellner and Asner 2009; Asner et al. 2013, 2014). Deviations from this stable range of observed λ values potentially provide another metric for detecting and mapping disturbance. In a recent study, repeat LiDAR collections permitted the quantification of positive height changes in a forest canopy in

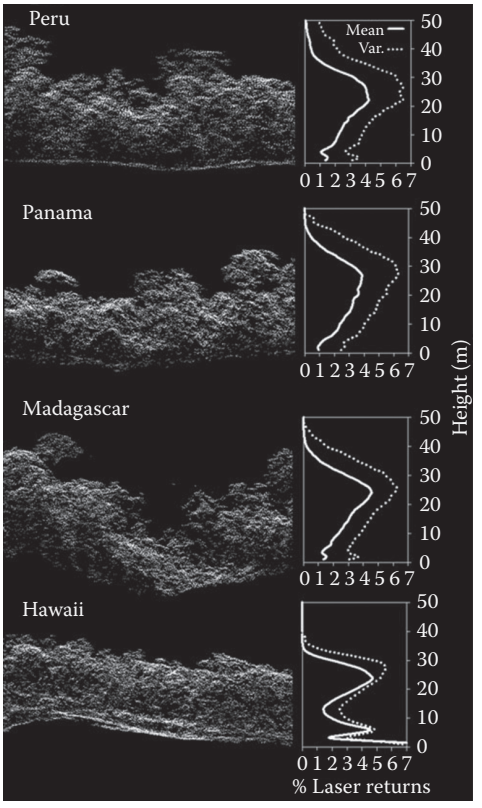

FIGURE 16.5 LiDAR cross-sectional views of four mature tropical forests in the Peruvian Amazon, Panamanian Neotropics, southeastern Madagascar, and Hawaii depict 3D forest structure along a 100 m long × 20 m wide transect. Right-hand panels show mean and spatial variance of LiDAR vertical canopy profiles for all returns in a 1 km² area centered on each cross section. Vertical canopy profiles are generally consistent across the four study sites, yet the Hawaiian forest contains the most pronounced groundcover, understory, and canopy layers. (Reprinted from Asner, G.P. et al., *Oecologia*, 168, 1147, 2012b).

Hawaii and illustrated how size and the proximity to other canopies influenced the outcome of competition for space within this forest (Kellner and Asner 2014).

16.5 Integrating HSI and LiDAR

In recent years, HSI and LiDAR observations have been integrated using two approaches. One method involves the acquisition of HSI and LiDAR data from separate platforms, such as from different aircraft, followed by modeling and analysis steps to fuse the resulting datasets (e.g., Mundt et al. 2006; Anderson et al. 2008; Jones et al. 2010). This is currently the most common approach, and following acquisition, the data must be digitally coaligned using techniques such as image pixel–based coregistration. These efforts usually yield an integrated data "cube" with an average misalignment of one pixel or so, although the scanning and/or array patterns of the HSI and LiDAR data may yield much higher coalignment errors.

A second, rapidly growing approach to HSI and LiDAR data integration involves the comounting of instruments on the same platform, whether on board aircraft or an unmanned aerial vehicle (UAV) (Asner et al. 2007). Integration steps range from colocating the instruments on the same mounting plate on board the aircraft or UAV, to precise time registration of each measurement, to final data fusion using ray tracing models for each instrument (Asner et al. 2012a). Each of these steps is key to producing a highly integrated dataset, reducing coalignment issues such that the data can be treated as one information vector per unit ground sample (e.g., one pixel). The onboard and postflight fusion of HSI and LiDAR data developed and deployed by the CAO (http://cao.carnegiescience.edu) has been replicated and is currently being used by the U.S. NEON's Airborne Operational Platform program (http://www.neoninc.org/science/aop).

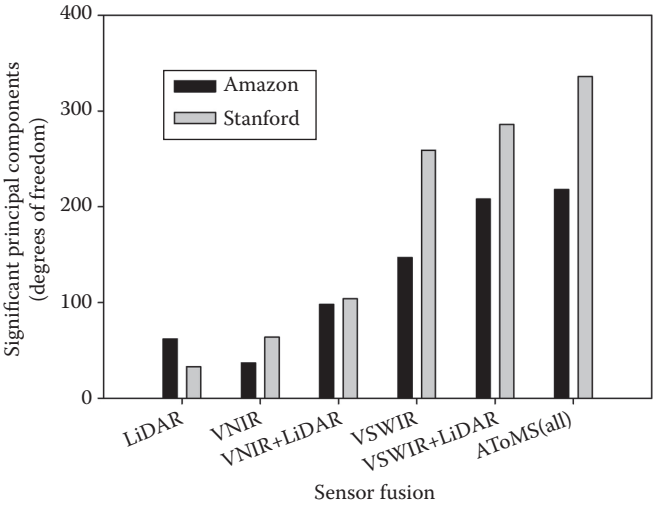

FIGURE 16.6 Integration of HSI and LiDAR sensor hardware, and data streams, provides a uniquely powerful way to greatly increase the inherent dimensionality of the data collected over forested areas and other ecosystems. For two sample 200 ha areas (Stanford University and a lowland Amazonian forest), individual LiDAR and HSI sensors provide highly dimensional data as assessed with principal components analysis. The dimensionality of the data increased when data are analyzed simultaneously. Here, VNIR is a visible-to-near infrared HSI and VSWIR is a visible-to-shortwave infrared HSI. All sensors combined are referred to as the Airborne Taxonomic Mapping Systems on board the CAO. (Reprinted from Asner, G.P., *Remote Sens. Environ.*, 124, 454, 2012a).

16.5.1 Benefits of Data Fusion

The benefits of HSI and LiDAR data fusion include increased data dimensionality, constraints on the interpretation of one portion of the dataset using another portion, and filtering of data to specific observation conditions or specifications. The dimensionality of, or degrees of freedom within, a fused dataset increases with the integration of complementary or orthogonal observations such as chemical or physiological metrics from HSI and structural or architectural measures from LiDAR. A highly demonstrative example can be taken from two integrated HSI–LiDAR datasets collected with the CAO Airborne Taxonomic Mapping System (Figure 16.6). One dataset was collected over a portion of Stanford University in 2011, and the other taken over a remote Amazonian rainforest in the same year. In the Stanford case, the LiDAR data alone contain about 25 degrees of freedom for a 200 ha area comprised buildings with varying architecture, vegetation ranging from grasses to trees, roads and pathways, and other built surfaces. Here, degrees of freedom are quantitatively assessed using principal component analysis, so each degree is orthogonal to or unique from the others (Asner et al. 2012a). A 72-band VNIR image of the same Stanford scene, taken from the same aircraft, contains about 50 degrees of freedom. Combined, the VNIR HSI and LiDAR provide about 100 degrees of freedom. A VSWIR imaging spectrometer on board the same aircraft provides about 260 degrees of freedom in the Stanford case. In conjunction, the LiDAR and VNIR and VSWIR HSI offer more than 330 orthogonally aligned sources of information. In the Amazon forest case, data fusion yields similar increases in data dimensionality, more than doubling the information content by sensor fusion over that which can be achieved by any one sensor.

A second powerful use of combined HSI and LiDAR data involves constraint of interpretation and/or filtering of one data stream relative to the other. Looking down upon a forest canopy, one observes strong variation in bright and dark portions of the canopy, as well as gaps and spectrally inconsistent observation conditions (Figure 16.7). As a result, reflectance analysis of forests is often an underdetermined problem involving variation in 3D architecture, leaf layering (LAI), and foliar biochemical constituents. This variation in illumination conditions occurs between pixels in high-resolution HSI data and within pixels in lower resolution HSI data. One of many possible ways to constrain observation conditions for improved HSI-based analysis of forest canopy traits is to use the LiDAR (Asner and Martin 2008; Dalponte et al. 2008; Colgan et al. 2012b). For example, LiDAR maps of top-of-canopy structure can be used to precisely model sun and viewing geometry on the canopy surface in each pixel. Combined with simple filtering of the HSI data based on the NDVI or other narrowband indices, an HSI image can be partitioned into regions most suitable for a particular type of analysis. Biochemical analyses are particularly sensitive to this filtering process, and much higher performances in biochemical retrievals can be achieved based on combined HSI–LiDAR filtering (Asner and Martin 2008). Still other approaches to integrate HSI and LiDAR data have yet to be explored, such as in the full 3D analysis and modeling of canopy structural and functional traits. These approaches will become more common with the rise of integrated data fusion systems.

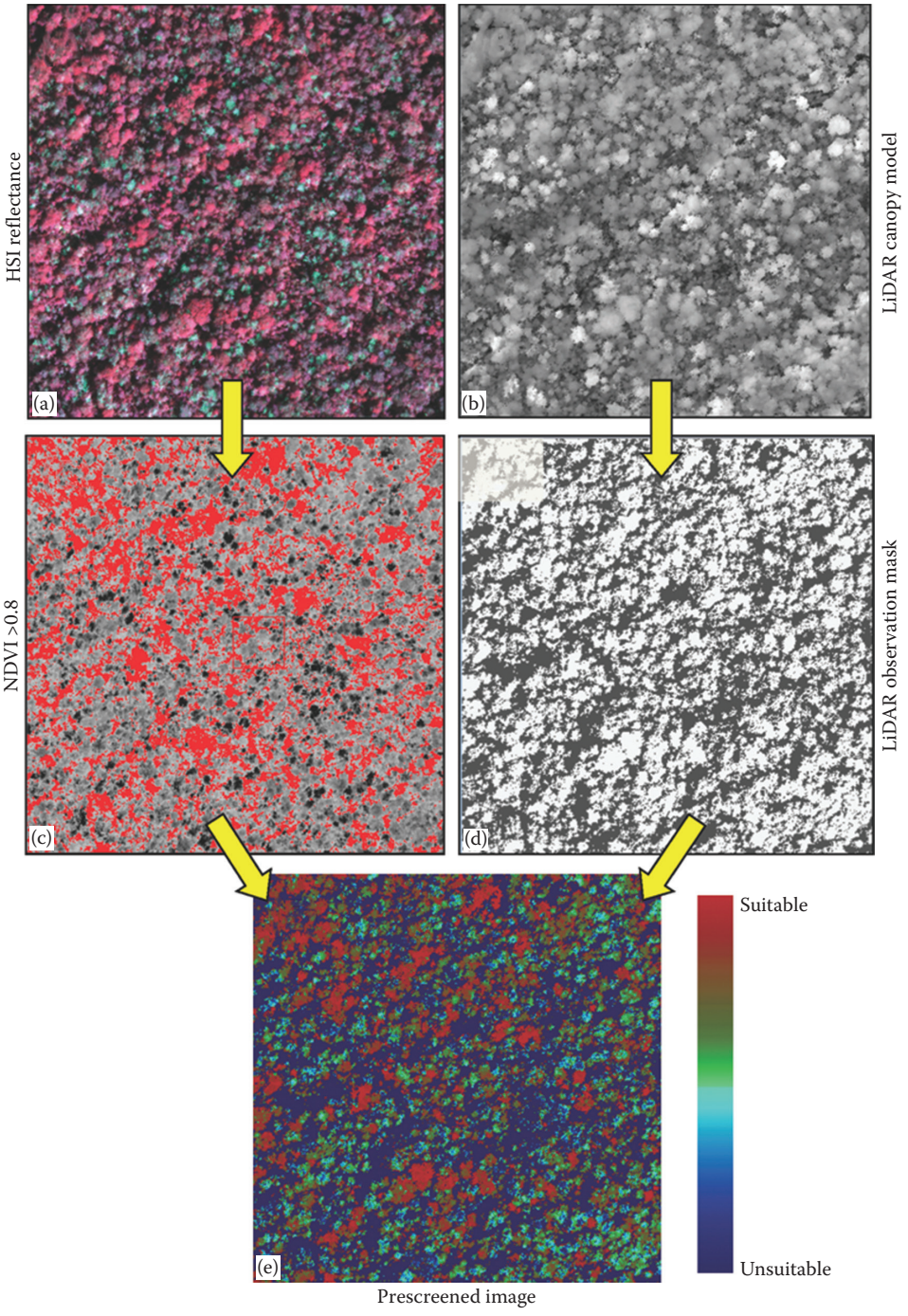

FIGURE 16.7 Prescreening of (a) HSI data using fused (b) LiDAR data. This can be accomplished in various ways, and an example is shown here. (c) A minimum NDVI threshold of 0.8 ensures sufficient foliar cover in the analysis. (d) Combining LiDAR and solar-viewing geometry, a filtering mask is generated to remove pixels in shade or of ground and water surfaces. (e) The resulting suitability image provides an indication of pixels that can be used for biophysical, biochemical, and/or physiological analysis.

16.6 Conclusions

HSI and LiDAR mapping provides independent and highly complementary data on forest canopies and whole ecosystems. Here, we summarized sources of HSI and LiDAR data, their general uses in determining forest structural and functional properties, and the potential value of collecting and analyzing HSI and LiDAR together via hardware integration and data fusion. Much of the science of HSI and LiDAR analysis of forests will remain in the airborne domain until orbital instrumentation is deployed and made available to the scientific research and application communities. In light of the myriad studies found throughout the remote sensing, forest science, and conservation research literature, it is clear that the time is right for a rapid expansion of HSI and LiDAR data collection and sharing efforts worldwide.

Acknowledgments

We thank E. Tasar for providing editing and management support. The CAO is made possible by the Gordon and Betty Moore Foundation, the Grantham Foundation for the Protection of the Environment, the John D. and Catherine T. MacArthur Foundation, the Avatar Alliance Foundation, the W. M. Keck Foundation, the Margaret A. Cargill Foundation, Mary Anne Nyburg Baker and G. Leonard Baker Jr., and William R. Hearst III.

References

Abshire, J. B., X. Sun, H. Riris, J. M. Sirota, J. F. McGarry, S. Palm, D. Yi et al. 2005. Geoscience laser altimeter system (GLAS) on the ICESat Mission: On-orbit measurement performance. *Geophys Res Lett* 32:L21S02.

Anderson, J. E., L. C. Plourde, M. E. Martin, B. H. Braswell, M-L. Smith, R. O. Dubayah, M. A. Hofton et al. 2008. Integrating waveform LiDAR with hyperspectral imagery for inventory of a northern temperate forest. *Remote Sens Environ* 112:1856–1870.

Armston, J., M. Disney, P. Lewis, P. Scarth, S. Phinn, R. Lucas, P. Bunting et al. 2013. Direct retrieval of canopy gap probability using airborne waveform LiDAR. *Remote Sens Environ* 134:24–38.

Asner, G. P. 1998. Biophysical and biochemical sources of variability in canopy reflectance. *Remote Sens Environ* 64:234–253.

Asner, G. P. 2013. Geography of forest disturbance. *Proc Nat/Acad Sci* 110:3711–3712.

Asner, G. P., C. Anderson, R. E. Martin, D. E. Knapp, R. Tupayachi, F. Sinca, and Y. Malhi. 2014. Landscape-scale changes in forest structure and functional traits along an andes-to-amazon elevation gradient. *Biogeosciences* 11:843–856.

Asner, G. P., J. K. Clark, J. Mascaro, G. A. Galindo García, K. Chadwick, D. A. Navarrete Encinales, G. Paez-Acosta et al. 2012c. High-resolution mapping of forest carbon stocks in the Colombian amazon. *Biogeosciences* 9:2683–2696.

Asner, G. P., R. F. Hughes, T. A. Varga, D. E. Knapp, and T. Kennedy-Bowdoin. 2009. Environmental and biotic controls over aboveground biomass throughout a tropical rain forest. *Ecosystems* 12:261–278.

Asner, G. P., R. F. Hughes, P. M. Vitousek, D. E. Knapp, T. Kennedy-Bowdoin, J. Boardman, R. E. Martin, M. Eastwood, and R. O. Green. 2008. Invasive plants alter 3-D structure of rainforests. *Proc Nat/Acad Sci* 105:4519–4523.

Asner, G. P., M. Keller, R. Pereira, J. C. Zweede, and J. N. Silva 2004b. Canopy damage and recovery after selective logging in Amazonia: Field and satellite studies. *Ecol Appl* 14:S280–S298.

Asner, G. P., J. R. Kellner, T. Kennedy-Bowdoin, D. E. Knapp, C. Anderson, and R. E. Martin. 2013. Forest canopy gap distributions in the southern Peruvian Amazon. *PloS One* 8:e60875.

Asner, G. P., D. E. Knapp, J. Boardman, R. O. Green, T. Kennedy-Bowdoin, M. Eastwood, R. E. Martin et al. B. 2012a. Carnegie airborne observatory-2: Increasing science data dimensionality via high-fidelity multi-sensor fusion. *Remote Sens Environ* 124:454–465.

Asner, G. P., D. E. Knapp, T. Kennedy-Bowdoin, M. O. Jones, R. E. Martin, J. Boardman and C. B. Field. 2007. Carnegie Airborne Observatory: In flight fusion of hyperspectral imaging and waveform light detection and ranging (LiDAR) for three-dimensional studies of ecosystems. *J Appl Remote Sens* 1:013536–36–21.

Asner, G. P. and D. B. Lobell. 2000. A biogeophysical approach for automated swir unmixing of soils and vegetation. *Remote Sens Environ* 74:99–112.

Asner, G. P. and R. E. Martin. 2008. Spectral and chemical analysis of tropical forests: Scaling from leaf to canopy levels. *Remote Sens Environ* 112:3958–3970.

Asner, G. P., R. E. Martin, R. Tupayachi, R. Emerson, P. Martinez, F. Sinca, G. V. N. Powell et al. 2011. Taxonomy and remote sensing of leaf mass per area (LMA) in humid tropical forests. *Ecol Appl* 21:85–98.

Asner, G. P. and J. Mascaro. 2014. Mapping tropical forest carbon: Calibrating plot estimates to a simple LiDAR metric. *Remote Sens Environ* 140:614–624.

Asner, G. P., J. Mascaro, H. C. Muller-Landau, G. Vieilledent, R. Vaudry, M. Rasamoelina, J. S. Hall et al. 2012b. A universal airborne LiDAR approach for tropical forest carbon mapping. *Oecologia* 168:1147–1160.

Asner, G. P., D. Nepstad, G. Cardinot, and D. Ray. 2004a. Drought stress and carbon uptake in an Amazon forest measured with spaceborne imaging spectroscopy. *Proc Nat/Acad Sci* 101:6039–6044.

Asner, G. P. and P. M. Vitousek. 2005. Remote analysis of biological invasion and biogeochemical change. *Proc Nat/Acad Sci* 102:4383–4386.

Asner, G. P. and A. S. Warner. 2003. Canopy shadow in IKONOS satellite observations of tropical forests and savannas. *Remote Sens Environ* 87:521–533.

Atherton, J. M., C. J. Nichol, M. Mencuccini, and K. Simpson. 2013. The utility of optical remote sensing for characterizing changes in the photosynthetic efficiency of Norway maple saplings following transplantation. *Int J Remote Sens* 34:655–667.

Baker, N. R. 2008. Chlorophyll fluorescence: A probe of photosynthesis in vivo. *Annu Rev Plant Biol* 59:89–113.

Baldeck, C. A., M. S. Colgan, J.-B. Féret, S. R. Levick, R. E. Martin, and G. P. Asner. 2014. Landscape-scale variation in plant community composition of an African savanna from airborne species mapping. *Ecol Appl* 24:84–93.

Barnsley, M. J., J. J. Settle, M. A. Cutter, D. R. Lobb, and F. Teston. 2004. The PROBA/CHRIS mission: A low-cost smallsat for hyperspectral multiangle observations of the earth surface and atmosphere. *IEEE Trans Geosci Remote Sens* 42:1512–1520.

Berry, J. A., C. Frankenberg, and P. Wennberg. 2013. New methods for measurements of photosynthesis from space. *Keck Institute for Space Studies* 1:72.

Bilger, W. and O. Björkman. 1990. Role of the xanthophyll cycle in photoprotection elucidated by measurements of light-induced absorbance changes, fluorescence and photosynthesis in leaves of *Hedera canariensis*. *Photosynth Res* 25:173–185.

Blackburn, G. A. 2007. Hyperspectral remote sensing of plant pigments. *J Exp Botany* 58:855–867.

Blair, J. B. and M. A. Hofton. 1999. Modeling laser altimeter return waveforms over complex vegetation using high-resolution elevation data. *Geophys Res Lett* 26:2509–2512.

Blair, J. B., D. L. Rabine, and M. A. Hofton. 1999. The laser vegetation imaging sensor: A medium-altitude, digitisation-only, airborne laser altimeter for mapping vegetation and topography. *ISPRS J Photogramm Remote Sens* 54:115–122.

Brokaw, N. V. L. 1985. Treefalls, regrowth, and community structure in tropical forests. In *The Ecology of Natural Disturbance and Patch Dynamics*, edited by S. T. A. Pickett, P. S. White (pp. 53–69). New York: Academic Press.

Bunting, P. and R. Lucas. 2006. The delineation of tree crowns in Australian mixed species forests using hyperspectral compact airborne spectrographic imager (CASI) data. *Remote Sens Environ* 101:230–248.

Bunting, P., R. Lucas, K. Jones, and A. R. Bean. 2010. Characterisation and mapping of forest communities by clustering individual tree crowns. *Remote Sens Environ* 114:231–245.

Chambers, J. Q., R. I. Negron-Juarez, D. M. Marra, A. Di Vittorio, J. Tews, D. Roberts, G. H. P. M. Ribeiro, S. E. Trumbore, and N. Higuchi. 2013. The steady-state mosaic of disturbance and succession across an old growth central amazon forest landscape. *Proc Nat/Acad Sci* 110:3949–3954.

Cheng, T., D. Riaño, A. Koltunov, M. L. Whiting, S. L. Ustin, and J. Rodriguez. 2013b. Detection of diurnal variation in orchard canopy water content using MODIS/ASTER airborne simulator (MASTER) data. *Remote Sens Environ* 132:1–12.

Cheng, Y.-B., E. M. Middleton, Q. Zhang, K. F. Huemmrich, P. K. E. Campbell, L. A. Corp, B. D. Cook et al. 2013a. Integrating solar induced fluorescence and the photochemical reflectance index for estimating gross primary production in a cornfield. *Remote Sens* 5:6857–6879.

Cho, M. A., J. A. van Aardt, R. Main, and B. Majeke. 2010. Evaluating variations of physiology-based hyperspectral features along a soil water gradient in a eucalyptus grandis plantation. *Int J Remote Sens* 31:3143–3159.

Clark, D. B. and D. A. Clark. 2000. Landscape-scale variation in forest structure and biomass in a tropical rain forest. *Forest Ecol Manag* 137:185–198.

Clark, M. L., D. A. Roberts, and D. B. Clark. 2005. Hyperspectral discrimination of tropical rain forest tree species at leaf to crown scales. *Remote Sens Environ* 96:375–398.

Colgan, M., C. Baldeck, J.-B. Féret, and G. Asner. 2012a. Mapping savanna tree species at ecosystem scales using support vector machine classification and BRDF correction on airborne hyperspectral and LiDAR data. *Remote Sens* 4:3462–3480.

Colgan, M. S., G. P. Asner, S. R. Levick, R. E. Martin, and O. A. Chadwick. 2012b. Topo-edaphic controls over woody plant biomass in South African savannas. *Biogeosciences* 9:1809–1821.

Curran, L. M., S. N. Trigg, A. K. McDonald, D. Astiani, Y. M. Hardiono, P. Siregar, I. Caniago, E. Kasischke. 2004. Lowland forest loss in protected areas of Indonesian Borneo. *Science* 303:1000–1003.

Dahlin, K. M., G. P. Asner, and C. B. Field. 2013. Environmental and community controls on plant canopy chemistry in a Mediterranean-type ecosystem. *Proc Nat/Acad Sci* 110:6895–6900.

Dalponte, M., L. Bruzzone, and D. Gianelle. 2007. Tree species classification in the Southern Alps based on the fusion of very high geometrical resolution multispectral/hyperspectral images and LiDAR data. *Remote Sens Environ* 123:258–270.

Dalponte, M., L. Bruzzone, and D. Gianelle. 2008. Fusion of hyperspectral and LiDAR remote sensing data for classification of complex forest areas. *IEEE Trans Geosci Remote Sens* 46:1416–1427.

Daughtry, C. S. T. 2001. Discriminating crop residues from soil by shortwave infrared reflectance. *Agronomy J* 93:125–131.

Daughtry, C. S. T., E. R. Hunt, P. C. Doraiswamy, and J. E. McMurtrey III. 2005. Remote sensing the spatial distribution of crop residues. *Agronomy J* 97:864–871.

Daughtry, C. S. T., C. L. Walthall, M. S. Kim, E. Brown de Colstoun, and J. E. McMurtrey III. 2000. Estimating corn leaf chlorophyll concentration from leaf and canopy reflectance. *Remote Sens Environ* 74:229–239.

Demmig-Adams, B. and W. W. Adams. 1996. The role of the xanthophyll cycle carotenoids in the protection of photosynthesis. *Trends Plant Sci* 1:21–26.

Demmig-Adams, B. and W. W. Adams. 2006. Photoprotection in an ecological context: The remarkable complexity of thermal energy dissipation. *New Phytol* 172:11–21.

Denslow, J. S. 1987. Tropical rainforest gaps and tree species diversity. *Annu Rev Ecol Evol Syst* 18:431–451.

Doughty, C. E., G. P. Asner, and R. E. Martin. 2011. Predicting tropical plant physiology from leaf and canopy spectroscopy. *Oecologia* 165:289–299.

Drake, J. B., R. O. Dubayah, D. B. Clark, R. G. Knox, J. B. Blair, M. A. Hofton, R. L. Chazdon et al. 2002. Estimation of tropical forest structural characteristics using large-footprint LiDAR. *Remote Sens Environ* 79:305–319.

Dubayah, R. and J. Drake. 2000. LiDAR remote sensing for forestry. *J For* 98:44–46.

Evans, J. R. 1989. Photosynthesis and nitrogen relationships in leaves of c3 plants. *Oecologia* 78:9–19.

Farquhar, G. D. and S. von Caemmerer. 1982. Modelling of photosynthetic response to environmental conditions. In *Physiological Plant Ecology II. Water Relations and Carbon Assimilation*, edited by O. L. Lange, P. S. Nobel, C. B. Osmond, and H. Ziegler (pp. 549–587). Berlin, Germany: Springer-Verlag.

Farquhar, G. D., S. von Caemmerer, and J. A. Berry. 1980. A biochemical model of photosynthetic CO_2 assimilation in leaves of c3 species. *Planta* 149:78–90.

Fassnacht, F. E., H. Latifi, A. Ghosh, P. K. Joshi, and B. Koch. 2014. Assessing the potential of hyperspectral imagery to map bark beetle-induced tree mortality. *Remote Sens Environ* 140:533–548.

Feilhauer, H., U. Faude, and S. Schmidtlein. 2011. Combining isomap ordination and imaging spectroscopy to map continuous floristic gradients in a heterogeneous landscape. *Remote Sens Environ* 115:2513–2524.

Feldpausch, T. R., J. Lloyd, S. L. Lewis, R. J. W. Brienen, M. Gloor, A. Monteagudo Mendoza, G. Lopez-Gonzalez et al. 2012. Tree height integrated into pantropical forest biomass estimates. *Biogeosciences* 9:3381–3403.

Féret, J.-B. and G. P. Asner. 2013. Spectroscopic classification of tropical forest species using radiative transfer modeling. *Remote Sens Environ* 115:2415–2422.

Féret, J.-B., C. François, G. P. Asner, A. A. Gitelson, R. E. Martin, L. P. R. Bidel, S. L. Ustin et al. 2008. Prospect −4 and −5: Advances in the leaf optical properties model separating photosynthetic pigments. *Remote Sens Environ* 112:3030–3043.

Féret, J.-B., C. François, A. Gitelson, G. P. Asner, K. M. Barry, C. Panigada, A. D. Richardson et al. 2011. Optimizing spectral indices and chemometric analysis of leaf chemical properties using radiative transfer modeling. *Remote Sens Environ* 115:2742–2750.

Field, C. and H. A. Mooney. 1986. The photosynthesis–nitrogen relationship in wild plants. In *On the Economy of Plant Form and Function*, edited by T. J. Givnish (pp. 25–55). Cambridge, U.K.: Cambridge University Press.

Field, C. B., J. T. Randerson, and C. M. Malmström. 1995. Global net primary production: Combining ecology and remote sensing. *Remote Sens Environ* 51:74–88.

Filella, I., A. Porcar-Castell, S. Munné-Bosch, J. Bäck, M. F. Garbulsky, and J. Peñuelas. 2009. PRI assessment of long-term changes in carotenoids/chlorophyll ratio and short-term changes in de-epoxidation state of the xanthophyll cycle. *Int J Remote Sens* 30:4443–4455.

Frankenburg, C., J. B. Fisher, J. Worden, G. Badgley, S. S. Saatchi, J-E. Lee, G. C. Toon et al. 2011. New global observations of the terrestrial carbon cycle from gosat: Patterns of plant fluorescence with gross primary productivity. *Geophys Res Lett* 38:L17706.

Gamon, G. A. and B. Bond. 2013. Effects of irradiance and photosynthetic downregulation on the photochemical reflectance index in Douglas-fir and ponderosa pine. *Remote Sens Environ* 135:141–149.

Gamon, J. A., J. Peñuelas, and C. B. Field. 1992. A narrow-waveband spectral index that tracks diurnal changes in photosynthetic efficiency. *Remote Sens Environ* 41:35–44.

Gamon, J. A., L. Serrano, and J. S. Surfus. 1997. The photochemical reflectance index: An optical indicator of photosynthetic radiation use efficiency across species, functional types, and nutrient levels. *Oecologia* 112:492–501.

Gamon, J. A. and J. S. Surfus. 1999. Assessing leaf pigment content and activity with a reflectometer. *New Phytol* 143: 105–117.

Gao, B. C. 1996. NDWI: A normalized difference water index for remote sensing of vegetation liquid water from space. *Remote Sens Environ* 58:257–266.

Gao, B. C. and A. F. H. Goetz. 1990. Column atmospheric water-vapor and vegetation liquid water retrievals from airborne imaging spectrometer data. *J Geophys Res Atmos* 95:3549–3564.

Gao, B. C. and A. F. H. Goetz. 1995. Retrieval of equivalent water thickness and information related to biochemical-components of vegetation canopies from AVIRIS data. *Remote Sens Environ* 52:155–162.

Garbulsky, M. F., J. Penuelas, J. Gamon, Y. Inoue, and I. Filella. 2011. The photochemical reflectance index (PRI) and the remote sensing of leaf, canopy and ecosystem radiation use efficiencies; a review and metaanalysis. *Remote Sens Environ* 115:281–297.

Gitelson, A. A. 2004. Wide dynamic range vegetation index for remote quantification of biophysical characteristics of vegetation. *J Plant Physiol* 161:165–173.

Gitelson, A. A., U. Gritz, and M. N. Merzlyak. 2003. Relationships between leaf chlorophyll content and spectral reflectance and algorithms for non-destructive chlorophyll assessment in higher plant leaves. *J Plant Physiol* 160:271–282.

Gitelson, A. A., Y. J. Kaufman, R. Stark, and D. Rundquist. 2002. Novel algorithms for remote estimation of vegetation fraction. *Remote Sens Environ* 80:76–87.

Gitelson, A. A., G. P. Keydan, and M. N. Merzlyak. 2006. Three-band model for noninvasive estimation of chlorophyll, carotenoids, and anthocyanin contents in higher plant leaves. *Geophys Res Lett* 33:L11402.

Gitelson, A. A., M. N. Merzlyak, and O. B. Chivkunova. 2001. Optical properties and non-destructive estimation of anthocyanin content in plant leaves. *J Photochem Photobiol* 74:38–45.

Gong, P., R. Pu, and I. R. Miller. 1992. Correlating leaf area index of ponderosa pine with hyperspectral CASI data. *Can J Remote Sens* 78:275–282.

Gong, P., R. Pu, and J. R. Miller. 1995. Coniferous forest leaf area index along the Oregon transect using compact airborne spectrographic imager data. *Photogramm Eng Remote Sensing* 61:107–117.

Green, R. O. 1998. Spectral calibration requirement for earth-looking imaging spectrometers in the solar-reflected spectrum. *Appl Optics* 37:683–690.

Green, R. O., V. Carrère, and J. E. Conel. 1989. Measurement of atmospheric water vapor using the airborne visible infrared imaging spectrometer. P. 6 in *Workshop Imaging Processing*, : Reno, NV: American Society of Photogrammetry and Remote Sensing.

Green, D. S., J. E. Erickson, and E. L. Kruger. 2003. Foliar morphology and canopy nitrogen as predictors of light-use efficiency in terrestrial vegetation. *Agric For Meteorol* 115:163–171.

Guanter, L., L. Alonso, L. Gómez-Chova, J. Amorós-López, J. Vila, and J. Moreno. 2007. Estimation of solar-induced vegetation fluorescence from space measurements. *Geophys Res Lett* 34:L08401.

Guerschman, J. P., M. J. Hill, L. J. Renzullo, D. J. Barrett, A. S. Marks, and E. J. Botha. 2009. Estimating fractional cover of photosynthetic vegetation, non-photosynthetic vegetation and bare soil in the Australian tropical savanna region upscaling the EO-1 hyperion and MODIS sensors. *Remote Sens Environ* 113:928–945.

Guo, J. and C. M. Trotter. 2004. Estimating photosynthetic light-use efficiency using the photochemical reflectance index: Variations among species. *Functional Plant Biol* 31:255–265.

Haboudane, D., J. R. Miller, N. Tremblay, P. J. Zarco-Tejada. 2002. Integrated narrow-band vegetation indices for prediction of crop chlorophyll content for application to precision agriculture. *Remote Sens Environ* 81:416–426.

Hernández-Clemente, R., R. M. Navarro-Cerrillo, and P. J. Zarco-Tejada. 2012. Carotenoid content estimation in a heterogeneous conifer forest using narrow-band indices and prospect + dart simulations. *Remote Sens Environ* 127:298–315.

Hilker, T., N. C. Coops, F. G. Hall, A. Black, M. A. Wulder, Z. Nesic, and P. Krishnan. 2008. Separating physiologically and directionally induced changes in PRI using BRDF models. *Remote Sens Environ* 112:2777–2788.

Homolová, L., Z. Malenovský, J. Clevers, G. García-Santos, and M. E. Schaepman. 2013. Review of optical-based remote sensing for plant trait mapping. *Ecol Complex* 15:1–16.

Huete, A. R. 1988. A soil-adjusted vegetation index (SAVI). *Remote Sens Environ* 25:295–309.

Hunt, E. R. Jr. and B. N. Rock. 1989. Detection of changes in leaf water content using near- and middle-infrared reflectances. *Remote Sens Environ* 30:43–54.

Hunt, E. R. Jr., S. L. Ustin, and D. Riaño. 2013. Remote sensing of leaf, canopy and vegetation water contents for satellite environmental data records. In *Satellite-based Applications of Climate Change*, edited by J. J. Qu, A. M. Powell, and M. V. K. Sivakumar (pp. 335–358). New York: Springer.

IPCC. 2000. Special report on land use, land-use change, and forestry. Edited by R. T. Watson, I. R. Noble, B. Bolin, N. H. Ravindranath, D. J. Verardo, and D. J. Dokeen, Cambridge, U.K.: Cambridge University Press.

Jacquemoud, S., W. Verhoef, F. Baret, C. Bacour, P. J. Zarco-Tejada, G. P. Asner, C. François, and S. L. Ustin. 2009. Prospect + sail: A review of use for vegetation characterization. *Remote Sens Environ* 113:S56–S66.

Joiner, J., Yoshida, Y., Vasilkov, A. P., and Middleton, E. M. 2011. First observations of global and seasonal terrestrial chlorophyll fluorescence from space. *Biogeosciences*, 8(3):637–651.

Jones, T. G., N. C. Coops, and T. Sharma. 2010. Assessing the utility of airborne hyperspectral and LiDAR data for species distribution mapping in the coastal Pacific Northwest, Canada. *Remote Sens Environ* 114:2841–2852.

Jordan, C. F. 1969. Leaf-area index from quality of light on the forest floor. *Ecology* 50:663–666.

Kalacska, M., S. Bohlman, G. A. Sanchez-Azofeifa, K. Castro-Esau, T. Caelli. 2007. Hyperspectral discrimination of tropical dry forest lianas and trees: Comparative data reduction approaches at the leaf and canopy levels. *Remote Sens Environ* 109:406–415.

Kattge, J., W. Knorr, T. Raddatz, and C. Wirth. 2009. Quantifying photosynthetic capacity and its relationship to leaf nitrogen content for global-scale terrestrial biosphere models. *Global Change Biol* 15:976–991.

Kefauver, S. C., J. Peñuelas, and S. Ustin. 2013. Using topographic and remotely sensed variables to assess ozone injury to conifers in the Sierra Nevada (USA) and Catalonia (Spain). *Remote Sens Environ* 139:138–148.

Kellner, J. R. and G. P. Asner. 2009. Convergent structural responses of tropical forests to diverse disturbance regimes. *Ecol Lett* 9:887–897.

Kellner, J. R. and G. P. Asner. 2014. Winners and losers in the competition for space in tropical forest canopies. *Ecol Lett*. doi:10.1111/ele.12256.

Kellner, J. R., D. B. Clark, S. P. Hubbell. 2009. Pervasive canopy dynamics produce short-term stability in a tropical rain forest landscape. *Ecol Lett* 12:155–164.

Kim, M. S. 1994. The use of narrow spectral bands for improving remote sensing estimation of fractionally absorbed photosynthetically active radiation (FAPAR). Masters Thesis, Department of Geography, University of Maryland, College Park, MD.

Knyazikhin, Y., P. Lewis, M. I. Disney, P. Stenberg, M. Mõttus, M. Rautiainen, P. Stenberg et al. 2013b. Reply to Ollinger et al.: Remote sensing of leaf nitrogen and emergent ecosystem properties. *Proc Nat/Acad Sci* 110:E2438–E2438.

Knyazikhin, Y., P. Lewis, M. I. Disney, P. Stenberg, M. Mõttus, M. Rautianinen, R. K. Kaufmann et al. 2013c. Reply to Townsend et al.: Decoupling contributions from canopy structure and leaf optics is critical for remote sensing leaf biochemistry. *Proc Nat/Acad Sci* 110:E1075–E1075.

Knyazikhin, Y., M. A. Schull, P. Stenberg, M. Mõttus, M. Rautiainen, Y. Yang, A. Marshak et al. 2013a. Hyperspectral remote sensing of foliar nitrogen content. *Proc Nat/Acad Sci* 110:E185–E192.

Kokaly, R. F. 2001. Investigating a physical basis for spectroscopic estimates of leaf nitrogen concentration. *Remote Sens Environ* 75:153–161.

Kokaly, R. F., G. P. Asner, S. V. Ollinger, M. E. Martin, and C. A. Wessman. 2009. Characterizing canopy biochemistry from imaging spectroscopy and its application to ecosystem studies. *Remote Sens Environ* 113:S78–S91.

Kokaly, R. F., B. W. Rockwell, S. L. Haire, and T. V. V. King. 2007. Characterization of post-fire surface cover, soils, and burn severity at the Cerro Grande fire, New Mexico, using hyperspectral and multispectral remote sensing. *Remote Sens Environ* 106:305–325.

le Maire, G., C. François, K. Soudani, D. Berveiller, J-Y. Pontailler, N. Bréda, H. Genet et al. 2008. Calibration and validation of hyperspectral indices for the estimation of broadleaved forest leaf chlorophyll content, leaf mass per area, leaf area index and leaf canopy biomass. *Remote Sens Environ* 112:3846–3864.

Lee, K.-S., W. B. Cohen, R. E. Kennedy, T. K. Maiersperger, and S. T. Gower. 2004. Hyperspectral versus multispectral data for estimating leaf area index in four different biomes. *Remote Sens Environ* 91:508–520.

Lefsky, M. A., W. B. Cohen, S. A. Acker, G. G. Parker, T. A. Spies, and D. Harding. 1999. LiDAR remote sensing of the canopy structure and biophysical properties of Douglas-fir western hemlock forests. *Remote Sens Environ* 70:339–361.

Lefsky, M. A., W. B. Cohen, D. J. Harding, G. G. Parker, S. A. Acker, and S. T. Gower. 2002. LiDAR remote sensing of above-ground biomass in three biomes. *Global Ecol Biogeogr.* 11:393–399.

Lefsky, M. A., D. J. Harding, M. Keller, W. B. Cohen, C. C. Carabajal, F. D. B. Espirito-Santo, M. O. Hunter et al. 2005. Estimates of forest canopy height and aboveground biomass using ICESat. *Geophys Res Lett* 35:L22S02.

Lewis, P. and M. Disney. 2007. Spectral invariants and scattering across multiple scales from within-leaf to canopy. *Remote Sens Environ* 109:196–206.

Lim, K., P. Treitz, K. Baldwin, I. Morrison, and J. Green. 2003. LiDAR remote sensing of forest structure. *Prog Phys Geog.* 27:88–106.

Lovell, J. L., D. L. B. Jupp, D. S. Culvenor, and N. C. Coops. 2003. Using airborne and ground-based LiDAR to measure canopy structure in Australian forests. *Can J Remote Sens* 29:607–622.

Magnussen, S., M. Wulder, and D. Seemann. 2002. Stand canopy closure estimated by line sampling. In *Continuous Cover Forestry*, edited by K. von Gadow, J. Nagel, and J. Saborowski (pp. 1–12). Dordrecht, the Netherlands: Springer.

Martin, M. E., S. D. Newman, J. D. Aber, and R. G. Congalton. 1998. Determining forest species composition using high spectral resolution remote sensing data. *Remote Sens Environ* 65:249–254.

Martin, M. E., L. C. Plourde, S. V. Ollinger, M.-L. Smith, B. E. McNeil. 2008. A generalizable method for remote sensing of canopy nitrogen across a wide range of forest ecosystems. *Remote Sens Environ* 112:3511–3519.

Meroni, M., M. Rossini, L. Guanter, L. Alonso, U. Rascher, R. Colombo, and J. Moreno. 2009. Remote sensing of solar-induced chlorophyll fluorescence: Review of methods and applications. *Remote Sens Environ* 113:2037–2051.

Middleton, E. M., Y.-B. Cheng, T. Hilker, T. A. Black, P. Krishnan, N. C. Coops, and K. F. Huemmrich. 2009. Linking foliage spectral responses to canopy-level ecosystem photosynthetic light-use efficiency at a Douglas-fir forest in Canada. *Can J Remote Sens* 35:166–188.

Montieth, J. L. 1977. Climate and the efficiency of crop production in Britain. *Philos Trans R Soc B* 281:277–294.

Morsdorf, F., B. Kötz, K. I. Itten, and B. Allgöwer. 2006. Estimation of LAI and fractional cover from small footprint airborne laser scanning data based on gap fraction. *Remote Sens Environ* 29:607–622.

Mundt, J. T., D. R. Streutker, and N. F. Glenn. 2006. Mapping sagebrush distribution using fusion of hyperspectral and LiDAR classifications. *Photogramm Eng Remote Sens* 72:47–54.

Muss, J. D., D. J. Mladenoff, and P. A. Townsend. 2011. A pseudo-waveform technique to assess forest structure using discrete LiDAR data. *Remote Sens Environ* 115:824–835.

Næsset, E. 2009. Effects of different sensors, flying altitudes, and pulse repetition frequencies on forest canopy metrics and biophysical stand properties derived from small-footprint airborne laser data. *Remote Sens Environ* 113:148–159.

Næsset, E. and T. Gobakken. 2008. Estimation of above- and below-ground biomass across regions of the boreal forest zone using airborne laser. *Remote Sens Environ* 112: 3079–3090.

Naidoo, L., M. A. Cho, R. Mathieu, and G. P. Asner. 2012. Classification of savanna tree species, in the greater Kruger national park region, by integrating hyperspectral and LiDAR data in a random forest data mining environment. *ISPRS J Photogramm Remote Sens* 69:167–179.

Naumann, J. C., J. E. Anderson, and D. R. Young. 2008. Linking physiological responses, chlorophyll fluorescence and hyperspectral imagery to detect salinity stress using the physiological reflectance index in the coastal shrub, *Myrica cerifera*. *Remote Sens Environ* 112:3865–3875.

Nelson, R. 1988. Estimating forest biomass and volume using airborne laser data. *Remote Sens Environ* 24:247–267.

Nepstad, D. C., A. Verissimo, A. Alencar, C. Nobre, E. Lima, P. Lefebvre, P. Schlesinger et al. 1999. Large-scale impoverishment of Amazonian forests by logging and fire. *Nature* 398:505–508.

Nichol, C. J., K. F. Huemmrich, T. A. Black, P. G. Jarvis, C. L. Walthall, J. Grace, and F. G. Hall. 2000. Remote sensing of photosynthetic-light-use efficiency of boreal forest. *Agric For Meteorol* 101:131:142.

Niinemets, U. 1999. Research review. Components of leaf dry mass per area—thickness and density—Alter leaf photosynthetic capacity in reverse directions in woody plants. *New Phytol* 144:35–47.

Ni-Meister, W., D. L. B. Jupp, and R. Dubayah. 2001. Modeling LiDAR waveforms in heterogeneous and discrete canopies. *IEEE Trans Geosci Remote Sens* 39:1943–1958.

Ollinger, S. V., P. B. Reich, S. Frolking, L. C. Lepine, D. Y. Hollinger, and A. D. Richardson. 2013. Nitrogen cycling, forest canopy reflectance, and emergent properties of ecosystems. *Proc Nat/Acad Sci* 110:E2437.

Ollinger, S. V., M. L. Smith, M. E. Martin, R. A. Hallett, C. L. Goodale, and J. D. Aber 2002. Regional variation in foliar chemistry and n cycling among forests of diverse history and composition. *Ecology* 83:339–355.

Parker, G. G. 1995. Structure and microclimate of forest canopies. In *Forest Canopies*, edited by M. D. Lowman and N. M. Nadkarni (pp. 73–106). New York: Academic Press.

Peñuelas, J., F. Baret, and I. Filella. 1995. Semiempirical indexes to assess carotenoids chlorophyll-a ratio from leaf spectral reflectance. *Photosynthetica* 31:221–230.

Peñuelas, J. F., J. Pinol, R. Ogaya, and I. Lilella. 1997. Estimation of plant water concentration by the reflectance water index WI (r900/r970). *Int J Remote Sens* 18:2869–2875.

Poorter, H., U. Niinemets, L. Poorter, I. J. Wright, and R. Villar. 2009. Causes and consequences of variation in leaf mass per area (LMA): A meta-analysis. *New Phytol* 182:565–588.

Popescu, S. C., R. H. Wynne, and R. F. Nelson. 2003. Measuring individual tree crown diameter with LiDAR and assessing its influence on estimating forest volume and biomass. *Can J Remote Sens* 29:564–577.

Rahman, A. F., J. A. Gamon, D. A. Fuentes, D. A. Roberts, and D. Prentiss. 2001. Modeling spatially distributed ecosystem flux of boreal forest using hyperspectral indices from AVIRIS imagery. *J Geophys Res* 106:33579–33591.

Reich, P. B., M. B. Walters, and D. S. Ellsworth. 1997. From tropics to tundra: Global convergence in plant functioning. *Proc Nat/Acad Sci* 94:13730–13734.

Riaño, D. P., F. Valladares, S. Condés, and E. Chuvieco. 2004b. Estimation of leaf area index and covered ground from airborne laser scanner (LiDAR) in two contrasting forests. *Agric For Meteorol* 124:269–275.

Riaño, D. P., P. Vaughan, E. Chuvieco, P. J. Zarco-Tejada, and S. L. Ustin. 2004a. Estimation of fuel moisture content by inversion of radiative transfer models to simulate equivalent water thickness and dry matter content. Analysis at leaf and canopy level. *IEEE Trans Geosci Remote Sens* 43:819–826.

Richardson, J. J., L. M. Moskal, and S.-H. Kim. 2009. Modeling approaches to estimate effective leaf area index from aerial discrete-return LiDAR. *Agric For Meteorol* 149:1152–1160. http://earthobservatory.nasa.gov/Features/EO1Tenth/

Riebeek, H. 2010. Earth observing-1: Ten years of innovation. In *NASA Earth Observatory: Features*.

Ripullone, F., A. R. Rivelli, R. Baraldi, R. Guarini, R. Guerrieri, F. Magnani, J. Peñuelas et al. 2011. Effectiveness of the photochemical reflectance index to track photosynthetic activity over a range of forest tree species and plant water statuses. *Funct Plant Biol* 38:177–186.

Roberts, D. A., P. Dennison, M. Gardner, Y. Hetzel, S. L. Ustin, and C. Lee. 2003. Evaluation of the potential of hyperion for fire danger assessment by comparison to the airborne visible infrared imaging spectrometer. *IEEE Trans Geosci Remote Sens* 41:1297–1310.

Roberts, D. A., M. Gardner, R. Church, S. L. Ustin, G. Scheer, and R. O. Green. 1998. Mapping chaparral in the Santa Monica mountains using multiple endmember spectral mixture models. *Remote Sens Environ* 65:267–279.

Roberts, D. A., S. L. Ustin, S. Ogunjemiyo, J. Greenberg, S. Z. Dobrowski, J. Chen, and T. M. Hinckley. 2004. Spectral and structural measures of northwest forest vegetation at leaf to landscape scale. *Ecosystems* 7:545–562.

Rondeaux, G., M. Steven, and F. Baret. 1996. Optimization of soil-adjusted vegetation indices. *Remote Sens Environ* 55:95–107.

Rouse, J. W., R. H. Haas, J. A. Schell, and D. W. Deering. 1974. Monitoring vegetation systems in the great plains with ERTS. In *Third ERTS Symposium NASA SP-351*, edited by S. C. Fraden, E. P. Marcanti, and M. A. Becker (pp. 309–317). Washington, DC: NASA.

Santos, M. J., J. A. Greenberg, and S. L. Ustin. 2010. Detecting and quantifying southeastern pine senescence effects to red-cockaded woodpecker (*Picoides borealis*) habitat using hyperspectral remote sensing. *Remote Sens Environ* 114:1242–1250.

Schull, M. A., S. Ganguly, A. Samanta, D. Huang, N. V. Shabanov, J. P. Jenkins, J. C. Chiu et al. 2007. Physical interpretation of the correlation between multi-angle spectral data and canopy height. *Geophys Res Lett* 34:L18405.

Schull, M. A., Y. Knyazikhin, L. Xu, A. Samanta, P. L. Carmona, L. Lepine, J. P. Jenkins et al. 2011. Canopy spectral invariants, part 2: Application to classification of forest types from hyperspectral data. *J Quant Spectrosc Radiat Transf* 112:736–750.

Sellers, P. J., S. O. Los, C. J. Tucker, C. O. Justice, D. A. Dazlich, G. J. Collatz, and D. A. Randall. 1996. A revised land surface parameterization (SiB2) for atmospheric GCMS. Part II: The generation of global fields of terrestrial biophysical parameters from satellite data. *J Climate* 9:706–737.

Serbin, S. P., D. N. Dillaway, E. L. Kruger, and P. A. Townsend. 2012. Leaf optical properties reflect variation in photosynthetic metabolism and its sensitivity to temperature. *J Exp Biol* 63:489–502.

Serrano, L., J. F. Peñuelas, and S. L. Ustin. 2002. Remote sensing of nitrogen and lignin in Mediterranean vegetation from AVIRIS data: Decomposing biochemical from structural signals. *Remote Sens Environ* 81:355–364.

Smith, M. L., M. E. Martin, L. Plourde, and S. V. Ollinger. 2003. Analysis of hyperspectral data for estimation of temperate forest canopy nitrogen concentration: Comparison between an airborne (AVIRIS) and a spaceborne (hyperion) sensor. *IEEE Trans Geosci Remote Sens* 41:1332–1337.

Smith, M. L., S. V. Ollinger, M. E. Martin, J. D. Aber, R. A. Hallett, and C. L. Goodale. 2002. Direct estimation of aboveground forest productivity through hyperspectral remote sensing of canopy nitrogen. *Ecol Appl* 12:1286–1302.

Soldberg, S., A. Brunner, K. H. Hanssen, H. Lange, E. Næsset, M. Rautiainen, and P. Stenberg. 2009. Mapping LAI in a Norway spruce forest using airborne laser scanning. *Remote Sens Environ* 113:2317–2327.

Somers, B. and G. P. Asner. 2013. Multi-temporal hyperspectral mixture analysis and feature selection for invasive species mapping in rainforests. *Remote Sens Environ* 136:14–27.

Spanner, M., L. Johnson, J. Miller, R. McCreight, J. Freemantle, J. Runyon, and P. Gong. 1994. Remote sensing of seasonal leaf area index across the Oregon transect. *Ecol Appl* 4:258–271.

Stylinksi, C. D., W. C. Oechel, J. A. Gamon, D. T. Tissue, F. Miglietta, and A. Raschi. 2000. Effects of lifelong [Co_2] enrichment on carboxylation and light utilization of Quercus pubescens Willd. Examined with gas exchange, biochemistry and optical techniques. *Plant Cell Environ* 23:1353–1362.

Sun, G. and K. J. Ranson. 2000. Modeling lidar returns from forest canopies. *IEEE Trans Geosci Remote Sens* 38:2617–2626.

Thenkabail, P. S, E. A. Enclona, M. S. Ashton, C. Legg, and M. J. De Dieu. 2004. Hyperion, IKONOS, ALI, and ETM+ sensors in the study of African rainforests. *Remote Sens Environ* 90:23–43.

Thomas, V., D. A. Flinch, J. H. McCaughey, T. Noland, L. Rich, and P. Treitz. 2006. Spatial modelling of the fraction of photosynthetically active radiation absorbed by a boreal mixedwood forest using a lidar—hyperspectral approach. *Agric For Meteorol* 140:287–307.

Thomas, V., J. H. McCaughey, P. Treitz, D. A. Finch, T. Noland, and L. Rich. 2009. Spatial modelling of photosynthesis for a boreal mixedwood forest by integrating micrometeorological, lidar, and hyperspectral remote sensing data. *Agric For Meteorol* 149:639–654.

Townsend, P. A. and J. R. Foster. 2002. Comparison of EO-1 hyperion to AVIRIS for mapping forest composition in the Appalachian mountains. *IGARSS* 2:793–795.

Townsend, P. A., S. P. Serbin, E. L. Kruger, and J. A. Gamon. 2013. Disentangling the contribution of biological and physical properties of leaves and canopies in imaging spectroscopy data. *Proc Nat/Acad Sci* 110:E1074.

Udayalakshmi, V., B. St-Onge, and D. Kneeshaw. 2011. Response of a boreal forest to canopy opening: Assessing vertical and lateral tree growth with multi-temporal LiDAR data. *Ecol Appl* 21:99–121.

Ustin, S. L., A. A. Gitelson, S. Jacquemoud, M. Schaepman, G. P. Asner, J. A. Gamon, and P. Zarco-Tejada. 2009. Retrieval of foliar information about plant pigment systems from high resolution spectroscopy. *Remote Sens Environ* 113: S67–S77.

Ustin, S. L., D. Riaño, and E. R. Hunt Jr. 2012. Estimating canopy water content from spectroscopy. *Isr J Plant Sci* 60:9–23.

Ustin, S. L. and A. Trabucco. 2000. Analysis of AVIRIS hyperspectral data to assess forest structure and composition. *J For* 98:47–49.

van Aardt, J. A. N., R. H. Wynne, and J. A. Scrivani. 2008. LiDAR-based mapping of forest volume and biomass by taxonomic group using structurally homogenous segments. *Photogramm Eng Remote Sens* 74:1033–1044.

Van den Berg, A. K. and T. D. Perkins. 2005. Nondestructive estimation of anthocyanin content in autumn sugar maple leaves. *HortScience* 40:685–686.

Vaughn, N. R., G. P. Asner, and C. P. Giardina. 2013. Polar grid fraction as an estimator of forest canopy structure using airborne lidar. *Int J Remote Sens* 34:7464–7473.

Vierling, K. T., L. A. Vierling, W. Gould, S. Martinuzzi, and R. Clawges. 2008. Lidar: Shedding new light on habitat characterization and modeling. *Front Ecol Environ* 6:90–98.

Waring, R. H. 1983. Estimating forest growth and efficiency in relation to canopy leaf area. *Adv Ecol Res* 13:327–354.

Weishampel, J. F., J. B. Blair, R. G. Knox, R. Dubayah, and D. B. Clark. 2000. Volumetric LiDAR return patterns from an old-growth tropical rainforest canopy. *Int J Remote Sens* 21:409–415.

Westoby, M., D. S. Falster, A. T. Moles, P. A. Vesk, and I. J. Wright. 2002. Plant ecological strategies: Some leading dimensions of variation between species. *Annu Rev Ecol Syst* 33:125–159.

White, J. C., N. C. Coops, T. Hilker, M. A. Wulder, and A. L. Carroll. 2007. Detecting mountain pine beetle red attack damage with EO-1 hyperion moisture indices. *Int J Remote Sens* 28:2111–2121.

Wolter, P. T., P. A. Townsend, B. R. Sturtevant, and C. C. Kingdon. 2008. Remote sensing of the distribution and abundance of host species for spruce budworm in Northern Minnesota and Ontario. *Remote Sens Environ* 112:3971–3982.

Wright, I. J., P. B. Reich, M. Westoby, D. D. Ackerly, Z. Baruch, F. Bongers, J. Cavender-Bares et al. 2004. The worldwide leaf economics spectrum. *Nature* 428:821–827.

Wulder, M. A., J. C. White, R. F. Nelson, E. Næsset, H. O. Ørka, N. C. Coops, T. Hilker et al. 2012. LiDAR sampling for large-area forest characterization: A review. *Remote Sens Environ* 121:196–209.

Zarco-Tejada, P. J., J. A. J. Berni, L. Suárez, G. Sepulcre-Cantó, F. Morales, and J. R. Miller. 2009. Imaging chlorophyll fluorescence from an airborne narrow-band multispectral camera for vegetation stress detection. *Remote Sens Environ* 113:1262–1275.

Zarco-Tejada, P. J., J. R. Miller, G. H. Mohammed, T. L. Noland, and P. H. Sampson 1999. Optical indices as bioindicators of forest condition from hyperspectral CASI data. *Proceedings of the 19th Symposium of the European Association of Remote Sensing Laboratories (EARSeL)*, Valladolid, Spain.

Zarco-Tejada, P. J., J. R. Miller, G. H. Mohammed, T. L. Noland, and P. H. Sampson. 2001. Scaling-up and model inversion methods with narrow-band optical indices for chlorophyll content estimation in closed forest canopies with hyperspectral data. *IEEE Trans Geosci Remote Sens* 39:1491–1507.

Zarco-Tejada, P. J., J. R. Miller, A. Morales, A. Berjón, and J. Agüera. 2004. Hyperspectral indices and model simulation for chlorophyll estimation in open-canopy tree crops. *Remote Sens Environ* 90:463–476.

Zarco-Tejada, P. J., A. Morales, L. Testi, and F. J. Villalobos. 2013. Spatio-temporal patterns of chlorophyll fluorescence and physiological and structural indices acquired from hyperspectral imagery as compared with carbon fluxes measured with eddy covariance. *Remote Sens Environ* 133:102–115.

Zhang, Y., J. M. Chen, J. R. Miller, and T. L. Noland. 2008. Leaf chlorophyll content retrieval from airborne hyperspectral remote sensing imagery. *Remote Sens Environ* 112:3234–3247.

Zimble, D. A., D. L. Evans, G. C. Carlson, R. C. Parker, S. C. Grado, and P. D. Gerard. 2003. Characterizing vertical forest structure using small-footprint airborne LiDAR. *Remote Sens Environ* 87:171–182.